STARS

University of Central Florida
STARS

Electronic Theses and Dissertations, 2004-2019

2008

Fundamental Study Of Fc-72 Pool Boiling Surface Temperature Fluctuations And Bubble Behavior

Alison Griffin
University of Central Florida

Showcase of Text, Archives, Research & Scholarship

FUNDAMENTAL STUDY
OF FC-72 POOL BOILING
SURFACE TEMPERATURE FLUCTUATIONS
AND BUBBLE BEHAVIOR

by

ALISON R. GRIFFIN

B.S.A.E. University of Central Florida, 2000
M.S.A.E. University of Central Florida, 2002

A dissertation submitted in partial fulfillment of the requirements
for the degree of Doctor of Philosophy in Mechanical Engineering
in the Department of Mechanical, Materials, and Aerospace Engineering
in the College of Engineering
at the University of Central Florida
Orlando, FL

Spring Term
2008

Major Professors: Ruey-Hung Chen and Louis C. Chow

ABSTRACT

A heater designed to monitor surface temperature fluctuations during pool boiling experiments while the bubbles were simultaneously being observed has been fabricated and tested. The heat source was a transparent indium tin oxide (ITO) layer commercially deposited on a fused quartz substrate. Four copper-nickel thin film thermocouples (TFTCs) on the heater surface measured the surface temperature, while a thin layer of sapphire or fused silica provided electrical insulation between the TFTCs and the ITO. The TFTCs were micro-fabricated using the liftoff process to deposit the nickel and copper metal films. The TFTC elements were 50 μm wide and overlapped to form a 25 μm by 25 μm junction. TFTC voltages were recorded by a DAQ at a sampling rate of 50 kHz. A high-speed CCD camera recorded bubble images from below the heater at 2000 frames/second. A trigger sent to the camera by the DAQ synchronized the bubble images and the surface temperature data.

As the bubbles and their contact rings grew over the TFTC junction, correlations between bubble behavior and surface temperature changes were demonstrated. On the heaters with fused silica insulation layers, 1-

2°C temperature drops on the order of 1 ms occurred as the contact ring moved over the TFTC junction during bubble growth and as the contact ring moved back over the TFTC junction during bubble departure. These temperature drops during bubble growth and departure were due to microlayer evaporation and liquid rewetting the heated surface, respectively. Microlayer evaporation was not distinguished as the primary method of heat removal from the surface.

Heaters with sapphire insulation layers did not display the measurable temperature drops observed with the fused silica heaters. The large thermal diffusivity of the sapphire compared to the fused silica was determined as the reason for the absence of these temperature drops. These findings were confirmed by a comparison of temperature drops in a 2-D simulation of a bubble growing over the TFTC junction on both the sapphire and fused silica heater surfaces. When the fused silica heater produced a temperature drop of 1.4°C, the sapphire heater produced a drop of only 0.04°C under the same conditions. These results verified that the lack of temperature drops present in the sapphire data was due to the thermal properties of the sapphire layer.

By observing the bubble departure frequency and site density on the heater, as well as the bubble departure diameter, the contribution of nucleate boiling to the overall heat removal from the surface could be calculated. These results showed that bubble vapor generation contributed to approximately 10% at 1 W/cm^2, 23% at 1.75 W/cm^2, and 35% at 2.9 W/cm^2 of the heat removed from a fused silica heater.

Bubble growth and contact ring growth were observed and measured from images obtained with the high-speed camera. Bubble data recorded on a fused silica heater at 3 W/cm^2, 4 W/cm^2, and 5 W/cm^2 showed that bubble departure diameter and lifetime were negligibly affected by the increase in heat flux. Bubble and contact ring growth rates demonstrated significant differences when compared on the fused silica and sapphire heaters at 3 W/cm^2. The bubble departure diameters were smaller, the bubble lifetimes were longer, and the bubble departure frequency was larger on the sapphire heater, while microlayer evaporation was faster on the fused silica heater. Additional considerations revealed that these differences may be due to surface conditions as well as differing thermal properties.

Nucleate boiling curves were recorded on the fused silica and sapphire heaters by adjusting the heat flux input and monitoring the local surface temperature with the TFTCs. The resulting curves showed a temperature drop at the onset of nucleate boiling due to the increase in heat transfer coefficient associated with bubble nucleation. One of the TFTC locations on the sapphire heater frequently experienced a second temperature drop at a higher heat flux. When the heat flux was started from 1 W/cm^2 instead of zero or returned to zero only momentarily, the temperature overshoot did not occur. In these cases sufficient vapor remained in the cavities to initiate boiling at a lower superheat.

ACKNOWLEDGMENTS

Thank you to my advisors Dr. Ruey-Hung Chen and Dr. Louis Chow, for letting me work on the same project for so many years and for letting me do it at my own pace. I truly appreciate you sticking with the project, and with me, until the heater and TFTCs finally worked! I have enjoyed my many years here at UCF thanks to you.

Thank you to my committee members, Dr. Kalpathy Sundaram and Dr. Kuo-Chi Lin, for all the years of help and interest in my research you have always provided. I am fortunate to have worked with you both.

Thank you to Arun Vijayakumar, for joining my committee, for your many hours in the lab, and for not giving up until my heater worked. You are the best!

Thank you to Dick Harris, for all your time and patience in the lab and for teaching me so much. What would I have done without you? I will really miss our visits. Best of luck with retirement, you deserve it!

TABLE OF CONTENTS

LIST OF FIGURES

LIST OF TABLES

LIST OF NOMENCLATURE

C_g Dissolved Gas Concentration (moles of gas/mole of liquid)

c_p Specific Heat (J/kg-K)

d_d Bubble Departure Diameter (μm)

f Bubble Frequency (bubbles/s)

h Heat Transfer Coefficient (W/m^2-K)

h_{fg} Latent Heat of Vaporization (J/kg)

H Henry's Constant (moles/mole-kPa)

I Current (amps)

L Length (mm)

n Bubble Site Density (sites/cm^2)

P Power (W)

P Pressure (Pa)

P_g Partial Gas Pressure (kPa)

P_t Total Pressure (kPa)

P_v Partial Vapor Pressure (kPa)

q'' Heat Flux (W/cm^2)

R Resistance (Ω)

R_{trans} Bubble Transition Radius (μm)

t	Thickness (mm)
ΔT	Surface Superheat (^{o}C)
T	Temperature (K)
T_w	Wall Temperature (K)
T_{sat}	Saturation Temperature (K)
t_g	Bubble Growth Time (ms)
t_w	Bubble Waiting Time (ms)
V	Voltage (V)
V_b	Bubble Volume (m^3)
α	Thermal Diffusivity (m^2/s)
α_l	Liquid Thermal Diffusivity (m^2/s)
ρ	Resistivity (Ω-mm)
ρ_l	Liquid Density (kg/m^3)
ρ_v	Vapor Density (kg/m^3)

INTRODUCTION

Technological improvements in fields such as electronic circuits and laser diodes have resulted in the development of more compact devices that produce higher power densities. Liquid to vapor phase change is considered to be the most favorable technique for high heat flux removal and protection against potentially hazardous temperature levels in these devices. Pool boiling is a two-phase heat transfer method that is capable of removing large amounts of heat from a surface. The pool boiling heat transfer mechanisms are complex, and as a consequence, many conflicting heat transfer models have been proposed [1]. A need for further investigation into the pool boiling heat removal mechanism still exists.

Pool boiling takes place in a submerged environment where bubbles nucleate from air or vapor trapped in cavities on the surface. Bubble nucleation begins when the surface superheat, defined as the difference between the wall surface temperature and the liquid saturation temperature, is increased until these cavities are activated. At low wall superheats, the heater surface is populated with non-interacting bubbles,

known as the individual bubble regime of pool boiling. As the surface superheat or the heat flux is increased, the number of activated sites also increases. The frequency of bubble formation and departure from a given nucleation site increases and vapor jets and columns eventually form. At still higher superheats, neighboring jets form large bubbles that merge laterally, trapping liquid between these bubbles and the surface. If this liquid completely evaporates before it can be replenished, a blanket of vapor forms over the surface. The heat removal from the surface is limited by the dry areas of the wall under this vapor blanket and a maximum heat flux occurs. This condition, called the critical heat flux (CHF), signifies the end of the nucleate boiling regime of the pool boiling curve [1]. For water pool boiling, CHF is known to be about 100 W/cm^2 [2]. The value of pool boiling CHF for FC-72 liquid, which has a high dielectric constant and is ideal for electronics cooling, is typically within the range of 16-20 W/cm^2 [3].

An individual pool boiling bubble growth cycle is shown in Figure 1 [1]. During the waiting period observed in Figure 1(a), energy from the superheated surface is transferred to the bulk fluid, forming a superheated thermal liquid layer. This increase in temperature causes the air or vapor trapped in a cavity to expand, as seen in Figure 1(b). In Figure 1(c), a

bubble emerges from the cavity and a thin layer of liquid called the

microlayer is trapped between the bubble and the surface. As the

bubble continues to grow, transferring heat from the surface and the

surrounding liquid at the liquid-vapor interface, the microlayer evaporates

until the surface under the bubble is dry, shown in Figure 1(d). In Figure

1(e), the bubble begins to lift off the surface. As the liquid-vapor-solid

contact ring shrinks, liquid rewets the previously dry areas. Once the

bubble has completely departed the surface, observed in Figure 1(f), the

waiting period begins again.
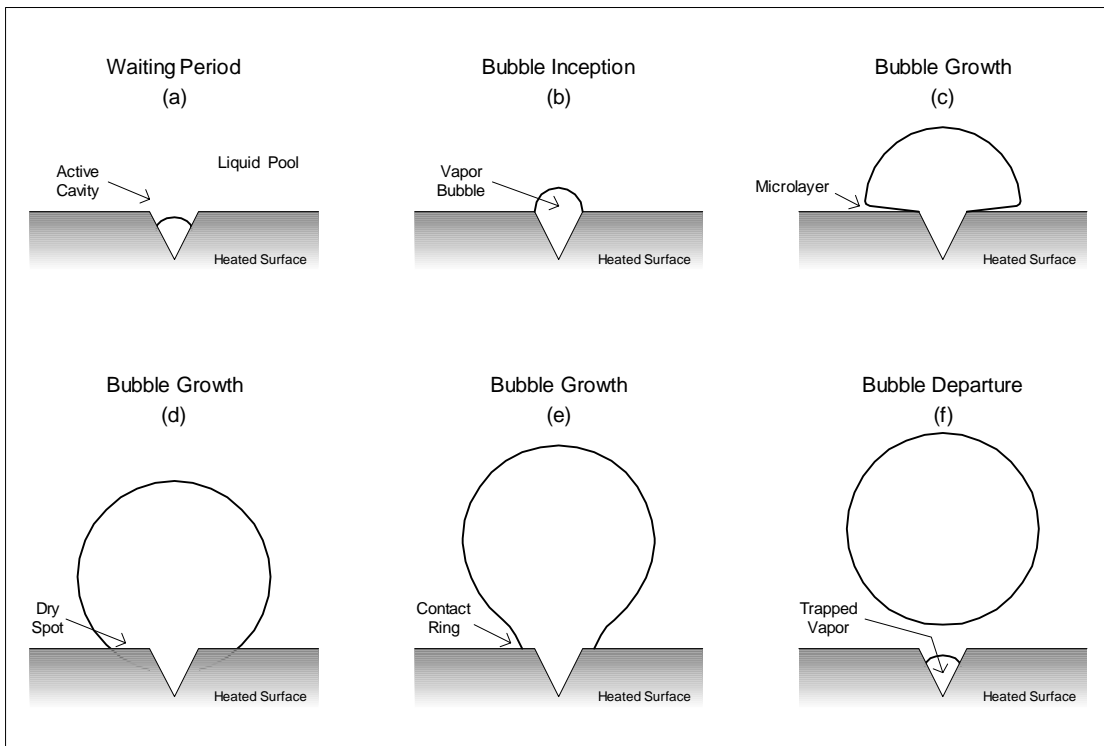
Figure 1: Bubble Growth Cycle

In this study, the pool boiling heat transfer mechanism was examined by analyzing the bubble behavior as well as the local temperature fluctuations caused by bubble nucleation, growth, and departure from a heated surface. While a variety of experimental devices have been used to study these temperature fluctuations, as detailed in the following background section, many unresolved issues remain that can be further explored with improved heater and temperature sensor designs. One such issue was the significance of microlayer evaporation and its contribution to the heat removal from a surface during nucleate boiling. The primary objective for this study was to develop a transparent heater capable of recording local surface temperature measurements under pool boiling bubbles. Thin film thermocouples with 25 μm by 25 μm junctions deposited on a heater composed of several transparent layers satisfied these conditions.

This novel heater design accomplished two main experimental goals. The first was a simultaneous observation of pool boiling bubbles and the corresponding temperature fluctuations associated with heat removal from the surface. The second was to obtain detailed information about bubble behavior, including growth rate, departure size, lifetime, and heat flux contribution, over the entire heater surface. These two areas were

studied under nucleate boiling conditions using the transparent heater with a 25 μm by 25 μm surface temperature resolution. FC-72, a highly wetting fluid with a 56°C saturation temperature, was used for these pool boiling experiments.

BACKGROUND

Many measurement techniques have been used to look at local

temperature and heat flux values under pool boiling conditions. In 1961,

Moore and Mesler [4] used a flush-mounted surface thermocouple to

record the surface temperature fluctuations under a single bubble in

water nucleate boiling. This surface thermocouple consisted of an Alumel

metal wire concentrically inserted through a Chromel metal tube, with the

wire electrically insulated from the tube. A thin nickel film deposited at

one end of the tube connected the wire and tube to form a 127 μm

diameter junction. This thermocouple had a response time of 1μs. The

temperature readings from these thermocouples were viewed on an

oscilloscope. The resulting temperature traces resembled the

temperature vs. time plot in Figure 2.   These temperature results showed a

rapid drop in temperature, approximately 20-30°F (10-17°C) over

approximately 2 ms. This temperature drop was followed by a gradual

temperature recovery before a second, smaller temperature drop

occurred. The temperature gradually increased again before the cycle

repeated itself. In a follow up experiment [5], one photograph of the

bubble during each bubble lifetime was taken from above the heater to

6

determine the size of the bubble at a certain time on the surface temperature trace. The boiling occurred at the thermocouple location from a single artificial cavity on a long nichrome strip about 1.5 mm thick.
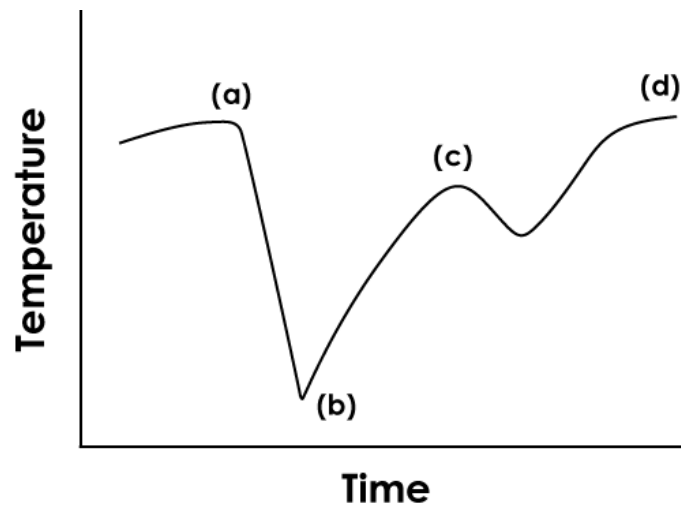
Figure 2: Surface Temperature Under Pool Boiling Bubble

By matching each bubble image to its corresponding location on a temperature trace like in Figure 2, a bubble growth cycle was observed. It was determined that the rapid temperature drop between (a) and (b) that occurred immediately after the bubble emerged from the cavity at (a) was due to the high heat removal associated with microlayer evaporation. After the microlayer was completely evaporated at (b), the dry surface under the bubble began to heat up. When the bubble departed from the surface at (c) and liquid rushed back in to rewet the

7

surface, the temperature dropped slightly again. Once that liquid was sufficiently reheated, the waiting time was over and a new bubble began to form at (d). A heat conduction analysis was also carried out over the area beneath a bubble to extract information about the local heat transfer rate. Based on the experiment parameters, the heat flux over the area under the bubble was calculated. For an input heat flux to the heater of about 50 W/cm^2, the local heat flux during the period of microlayer evaporation was found to be about 300 W/cm^2. This result suggests that the local heat flux beneath a bubble can be nearly an order of magnitude higher than the heater-averaged value. The high local heat flux was attributed to rapid evaporation of the microlayer.

Cooper and Lloyd [6] in 1969 developed a device with six germanium thin film thermometers, as small as 75 μm by 75 μm each, which measured the surface temperatures as a single pool boiling bubble successively grew over each thermometer. These thin film thermometers were 0.25-0.5 μm thick and had a time constant of around 10^{-8} seconds. The sampling rate of the temperature data was limited to 1000 Hz by the equipment resolution. The four middle thermometers, each spaced 1.5 mm apart in a linear pattern, were used to measure temperature, and one of the two outside thermometers had a current pulse passed through it to produce a

bubble. Organic fluids that did not conduct electricity, such as toluene and isopropyl alcohol, were used in this experiment at varying pressures. Glass and ceramic plates were used as the substrate materials. A camera provided a side view of the bubbles to observe bubble growth and departure and to interpret the simultaneous temperature fluctuations. Only sketches of these high-speed photographs were presented, again similar to Figure 2. The temperature results from this experiment also showed a steep temperature drop at (a) as the bubble moved over the thermometer, suggesting microlayer evaporation as the bubble grew larger. A slower increase in temperature occurred after the microlayer was evaporated at (b) and the thermometer was located under the bubble where the wall was dry. A temperature drop at (c), smaller than the first one at (a), took place as the bubble departed and liquid covered the thermometer, and the temperature slowly increased before the next bubble was formed at (d). A one-dimensional heat conduction analysis was performed using the temperature traces to determine the heat flux under a bubble. It was calculated that the heat flux from the surface peaked when the temperature was at its lowest point, which occurred at the end of the microlayer evaporation period.

More modern fabrication techniques, as well as higher resolution data acquisition and imaging systems, have been used in the last decade to continue the examination of pool boiling heat transfer. Sako and Kikuchi [7] fabricated eight copper-nickel thin film thermocouples (TFTCs) to monitor the surface temperature fluctuations over a 10 mm by 10 mm heated area. These TFTCs were 0.3 μm thick, had a junction size of 50 μm by 200 μm, and were each 1mm apart. A 10 mm square nichrome film deposited on the bottom surface of the glass substrate served as the heat source. This non-transparent nichrome film completely covered the heated area, so bubbles were viewed from the side with a high-speed camera synchronized with the temperature fluctuations. These temperature results from this experiment, recorded at low pressures in an n-hexane fluid, were similar to the results of Moore and Mesler [4] and Cooper and Lloyd [6] as previously described. A large temperature drop due to microlayer evaporation, followed by a gradual temperature increase and then another temperature drop as the bubble departed and bulk liquid replaced the bubble. A one-dimensional heat conduction analysis was also performed to determine the amount of heat removed from the surface based on the temperature fluctuations. The calculations showed that the thermocouples further away from the bubble inception site measured a lower peak heat flux, but a greater total heat removal,

from the surface. In addition, a general observation was made from the side-view bubble images; that the two temperature drops occurred when the outer edge of the bubble crossed the thin film thermocouple during growth and again during departure.

Other types of devices have been used as well to look at surface temperature phenomenon during pool boiling. Some of these studies more closely examined the theory, supported by the three previously described experiments, that microlayer evaporation is the dominant heat transfer mechanism during pool boiling. Experiments by Yaddanapudi and Kim [8], Demiray and Kim [9], and Myers et al. [10] used an array of 96 microheaters arranged in a 10 x 10 pattern to monitor local heat flux under constant surface temperature conditions or local surface temperature under constant surface heat flux conditions. These microheaters were platinum resistance heaters deposited on quartz and silica substrates. The entire heater array was 2.7 mm by 2.7 mm when the microheaters were each 270 μm by 270 μm [8] and 1 mm by 1 mm when the microheaters were each 100 μm by 100 μm [9, 10]. The pattern of the resistance heaters covered approximately 50% of the heater surface, so these devices were considered to be semi-transparent and allowed the bubble to be viewed from below the heater. Bubble images were

also recorded from the side with a high-speed camera. All of the experiments were done at atmospheric pressure using saturated FC-72. The first two experiments [8, 9] measured the heat transfer under single pool boiling bubbles. The heater resistance combined with direct measurements of the voltage across the heaters calculated the power dissipation under a constant surface temperature. The data acquisition system and high speed camera recorded synchronized heat transfer measurements at 3704 Hz and bubble images at 3704 frames/second, respectively. By comparing the heat transferred from the surface with the latent heat associated with the bubble, it was determined that only about 12.5% of the energy in the bubble came from microlayer evaporation; the rest was due to transient conduction from the superheated liquid layer. The third experiment [10] measured the temperature under pool boiling bubbles under constant heat flux conditions. The data sampling rate was 1130 Hz, corresponding to the 1130 frames/second camera rate. The temperature measurements reported were not at specific locations under the bubble, but rather averaged over the entire heater array. Surface temperature fluctuations over the whole bubble area were generated by the growth and departure of single bubbles. Unlike previous studies that measured temperature drops during bubble growth and departure over a localized temperature sensor, the temperature drops in this study were

12

only observed to occur during bubble departure. The average temperature actually increased during bubble growth due to the heat transfer to the dry spot. The heat removal from the surface was also numerically calculated from the temperature data. These heat transfer results exhibited a decrease during bubble growth and an increase during bubble departure, implying that microconvection and transient conduction into the rewetting liquid, not microlayer evaporation, were the primary heat removal methods. It was determined that only about 23% of the heat transferred from the wall was removed by microlayer evaporation.

A study by Moghaddam and Kiger [11] involved a heater comprised of layers of silicon, silicon oxide/nitride, benzocyclobutene, RTD sensors, and a thin film heat source on the bottom of the substrate. The heater was 3.6 mm x 3.6 mm and 71 μm thick. The 44 temperature sensors were deposited 0.5 μm below the pool boiling surface in a radial pattern and had 22-40 μm spatial resolution. Temperature measurements were recorded at 8 kHz under individual bubbles formed from artificial cavities on the heater surface while side-view images of the bubbles were taken with a high-speed camera at 8000 frames/second. In this experiment, a single bubble grew over five successive temperature sensors. Each sensor

registered a temperature drop during bubble growth, attributed to microlayer evaporation, and each sensor registered a temperature drop during bubble departure, attributed to the FC-72 liquid rewetting the surface. The bubble observations suggested that the liquid/vapor/solid contact line directly caused the temperature drops. The temperature information from each sensor was input into a numerical model to determine the heat flux associated with each temperature drop. By comparing the energy in the microlayer to the total energy in the bubble, the contribution of microlayer evaporation to the bubble was calculated to be 14.7%, similar to the 12.5% found in a previous study [9] described above. Microlayer evaporation and transient conduction while the liquid rewets the surface during bubble departure had similar contributions to the total heat transfer from the surface.

A type of temperature sensor called a microthermocouple was used by Buchholz et al. [12] to measure surface temperature changes over the entire pool boiling curve. The two elements of the microthermocouples were a constantan wire and a 2.5 μm thick copper film that formed a 38 μm thermocouple junction. There were 36 microthermocouples placed in a 1 mm^2 area and positioned 3.6 μm below the surface of the copper heater. The thermocouple temperatures were recorded at a 25 kHz

frequency. Camera images were not taken in this experiment. Nucleate boiling tests in isopropanol and FC-3284 were performed and temperature fluctuations due to bubble growth, suggesting a high local heat flux under the bubbles, were observed. The frequency and magnitude of these temperature drops, and therefore the contribution of nucleate boiling to the overall heat removal, increased with an increasing surface superheat.

Some previous pool boiling experiments used transparent or semi-transparent heaters for primarily visual studies of pool boiling bubbles. These experiments did not record localized surface temperature measurements, although some monitored the average heater surface temperature. One example of this type of experiment was performed by Rini et al. [3] using a heater with a 1 cm by 1 cm semi-transparent synthetic diamond substrate. A thin film Ni-Cr resistor deposited on the bottom surface of the heater served as the heat source. This resistor pattern covered approximately half of the viewing area of the heater, where bubbles could be observed between the gaps in the pattern. Bulk wire thermocouples mounted to the bottom surface of the heater recorded only the average temperature on the heater surface. This pool boiling experiment was conducted at atmospheric pressure using FC-72 as the fluid. Bubble properties were documented with a high-speed

camera positioned below the heater under varying heat flux conditions. Bubble departure diameter did not change with an increase in the heat flux, while the bubble lifetime decreased with an increase in heat flux. The heat removal contribution of nucleate boiling was calculated at both low and high heat flux levels. The nucleate boiling contribution was 35% and 73% at 1 W/cm^2 and 10 W/cm^2, respectively.

The measurement device that was developed in the current study is the first that is completely transparent while measuring the local surface temperature, allowing clear bubble images to be obtained from below the heater and for bubble behavior to be closely observed. In addition, this experiment incorporated many of the advantages of the previous experiments described above. The thermocouple junctions were of a similar or smaller size than all of the preceding temperature sensors, providing excellent spatial resolution and fast response time. The data sampling rate and camera frame rate were as high, or higher, than the prior experiments in order to capture the details of the temperature fluctuations and corresponding bubble growth. This experiment was the first to record bubble images from underneath a transparent heater at high frame rates while sampling small, synchronized temperature sensors at a very high frequency.

EXPERIMENTAL DESIGN

A transparent heater was designed to observe the bubbles that form on the top of a heated surface during pool boiling experiments. A camera positioned below the heater viewed these bubbles at a high frame rate to capture the details of the bubble behavior. Thin film thermocouples (TFTCs) deposited on the heater measured the temperature fluctuations caused by heat removal from the surface due to microlayer evaporation during bubble growth and rewetting of the surface during bubble departure. These temperature fluctuations were recorded simultaneously with the bubble images to correlate surface temperature and bubble behavior under pool boiling conditions.

Heater

The 17 mm by 17 mm heater was composed of multiple layers, as seen in Figure 3. The base of the heater was a 0.5 mm thick fused quartz substrate with greater than 90% optical transmittance. A conductive layer of indium tin oxide (ITO) was deposited over the entire quartz substrate to serve as a power source for the heater. Attempts to deposit the ITO in the

on-campus microfabrication lab led to non-uniform films that produced

inconsistent boiling patterns. Instead the ITO was commercially deposited

by Evaporated Coatings Inc. to ensure uniform film thickness, and

therefore uniform boiling. These ITO films were fabricated with a sheet

resistance of 64 Ω/square. The final resistance of the ITO after TFTC

fabrication was typically about 40 Ω. ITO has a 90-95% optical

transmittance, and therefore the combination of substrate and heat

source was essentially transparent. This transparency allowed

observations of the top surface of the heater to be made from below the

heater.

TFTC Junction

Cu   **Ni**

Al   **Sapphire / Fused Silica**   **Al**

ITO

Fused Quartz
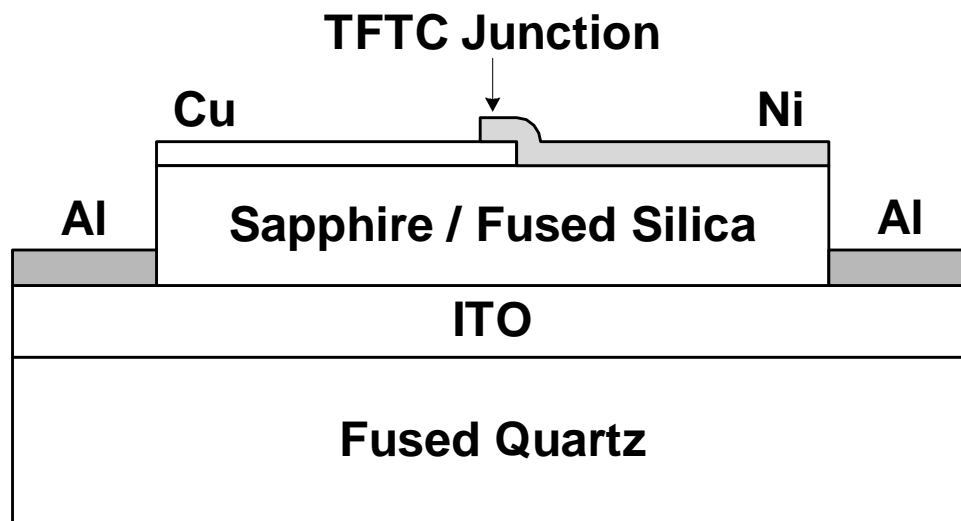
Figure 3: Side View Cross-Section of Heater

Two aluminum power pads, each 2.5 mm by 10 mm and 100 nm thick, were deposited on opposite sides of the heater. Power was supplied to the ITO by wires epoxied to these aluminum films. These power pads can be observed in an overhead view of the heater, shown in Figure 4.
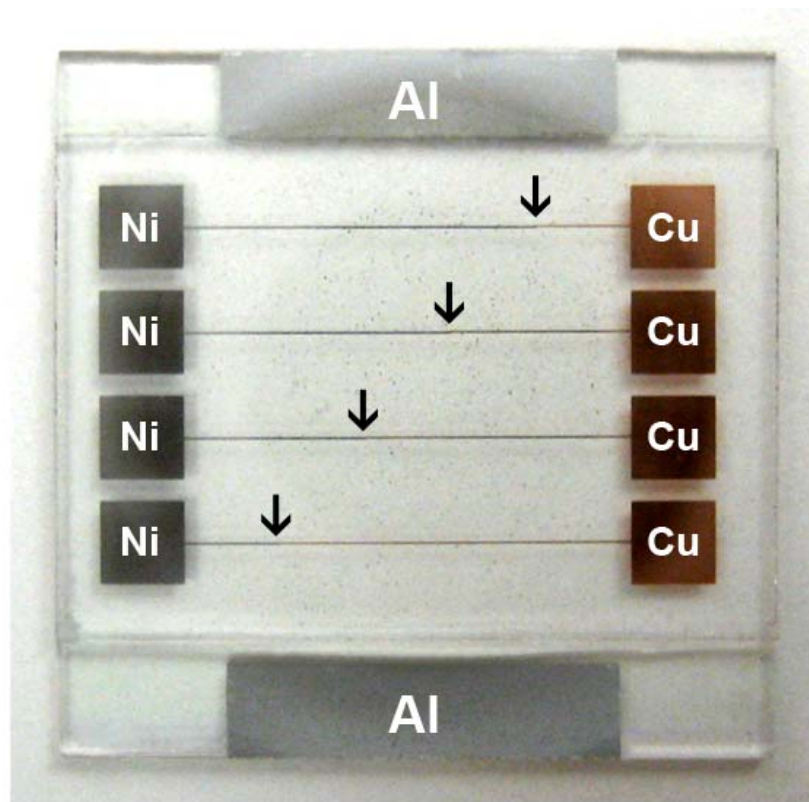
Figure 4: Top View Photograph of Heater

An additional layer between the ITO film and the thin film thermocouples proved to be necessary to provide electrical insulation. Efforts were made to deposit thin layers of aluminum oxide and silicon oxide for insulation,

but possible pinholes or film thickness issues prevented these oxide layers from protecting the TFTCs from the ITO. Instead, layers of 0.2 mm thick sapphire and 0.1 mm thick synthetic fused silica were successfully used for electrical insulation. These layers were mounted to the top of the ITO with optical cement that was cured under an ultraviolet light. The sapphire and fused silica layers covered the 12 mm by 17 mm area between the aluminum power pads. This entire configuration of quartz, ITO, cement, and the insulation layer was essentially transparent (greater than 90% optical transmittance) below the heated area.

<u>Thin Film Thermocouples</u>

Thin film thermocouples (TFTCs) were designed to monitor the surface temperature fluctuations that occur during pool boiling due to bubble nucleation, growth, and departure. The four TFTCs, each composed of a copper and a nickel element, were deposited on top of the insulation layer. Each component of the TFTC was 50 μm wide, and the two metal films overlapped to form 25 μm by 25 μm junctions, as seen in Figure 5.
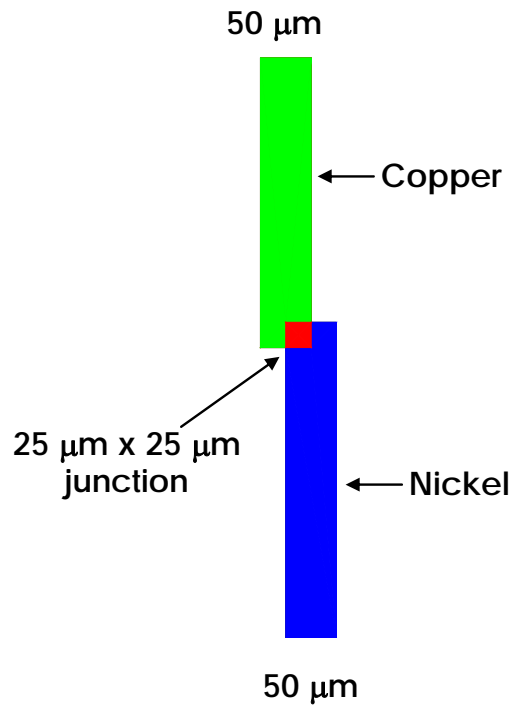
Figure 5: Overlap of TFTC Junction

TFTC Deposition

The thin film thermocouples were deposited on the top insulation layer of the heater by a lift-off process. This deposition was completed in the UCF microfabrication clean room facility. To deposit the copper side of the TFTCs, first negative photoresist was applied to the substrate surface by a spin-on method. The sample was then soft-baked at 150°C for one minute. A clear-field mask of the copper TFTC elements, shown in Figure

6, was positioned on the substrate with a mask aligner and was exposed to ultraviolet light for about ten seconds. The UV light physically altered the exposed photoresist region.
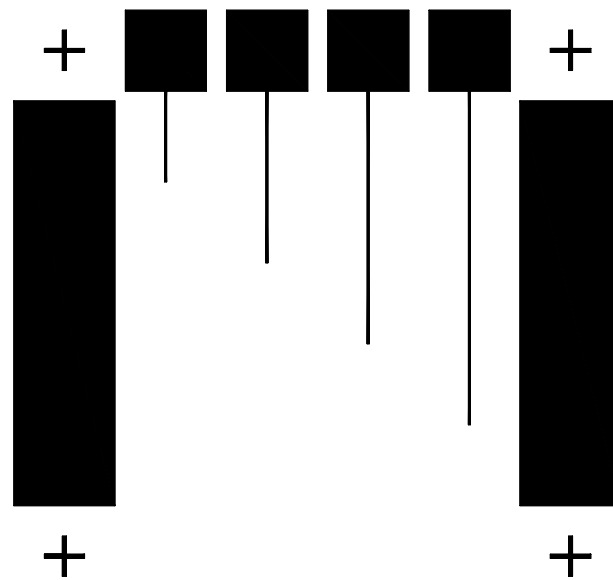
Figure 6: Copper TFTC Deposition Mask

The sample was then baked again at 100°C for one minute. The substrate was next placed in a developing solution for one minute to remove the areas of photoresist that had been covered by the mask pattern and unaffected by the UV light. This left a layer of photoresist everywhere on the heater except for the locations of the copper TFTC elements. The substrate was placed in a vacuum chamber where a 40 nm thick blanket

of copper was evaporated onto the entire surface. This evaporation

process took approximately 1-2 minutes in a 3×10^{-5} Torr vacuum. When it

was removed from the vacuum, the substrate was placed in an acetone

solution to remove the remaining photoresist and the copper layer

covering it. The only material left on the substrate was the copper pattern

of the TFTCs. This metal lift-off process was repeated to create the nickel

side of the TFTC using a clear-field mask of the nickel pattern. Figure 7

shows this pattern of the mask used for nickel deposition. Using a mask

aligner to match up the placement marks on the corners of the two masks

ensured that the copper and nickel films overlapped to form the

preferred junction size.
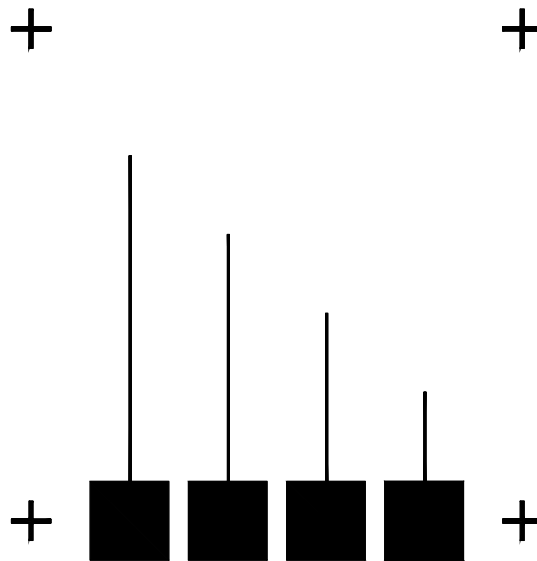
Figure 7: Nickel TFTC Deposition Mask

Figure 8 shows a photograph of an actual TFTC junction taken with an optical profilometer. It can be observed, though, that for this particular TFTC, the overlap junction is actually slightly larger than 25 μm by 25 μm due to the sensitive mask alignment procedure.
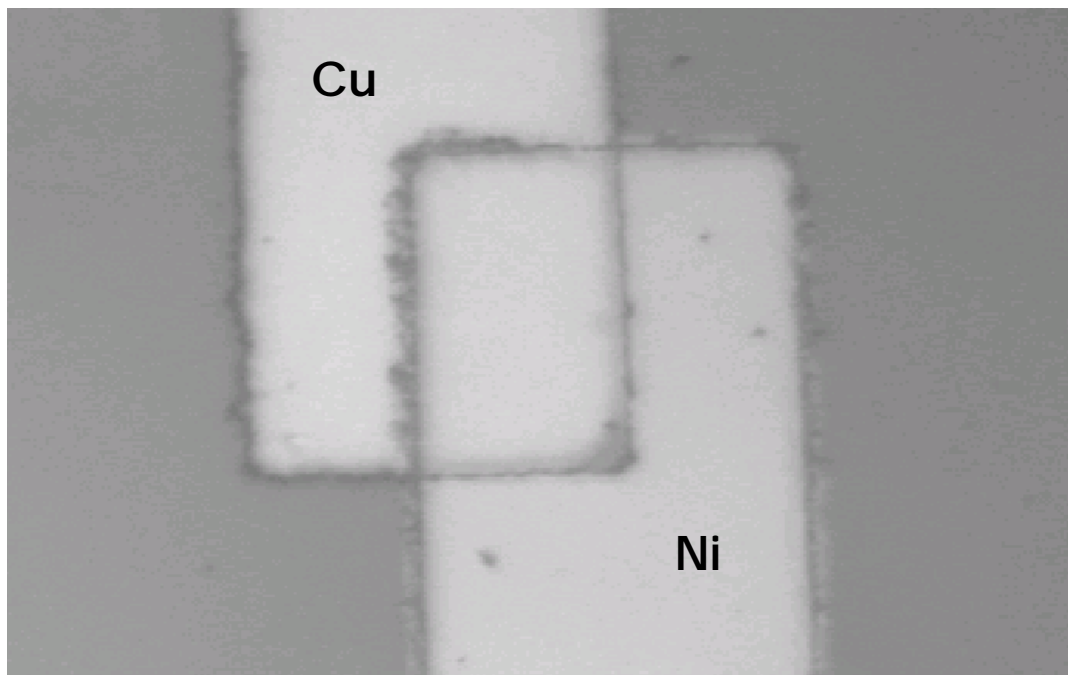
Figure 8: Photograph of TFTC Junction

The power pad pattern located in the copper mask seen in Figure 6 was not used in the final heater fabrication process due to the step in thickness introduced to the heater by the insulation layer. Instead a similar lift-off method was used in a separate process to deposit the aluminum power pads directly on top of the ITO power source.

An overhead view of a completed heater can be previously seen in Figure 4, where the arrows indicate the locations of the TFTC junctions. The TFTC junctions were staggered so that boiling on different areas of the heated surface could be observed and measured. The 2 mm by 2 mm squares on the opposite sides of the heater from the power pads are the thermocouple pads. Thin copper and nickel wires were epoxied to these copper and nickel pads with an electrically conducting silver epoxy that cured overnight at room temperature. Both components of the silver epoxy were weighed with a precision balance before mixing to ensure uniform epoxy composition and consistency when cured.   Soldering was also successfully used to attach power wires to the power pads, but soldered TFTC wires did not produce stable voltage measurements and therefore soldering was eliminated as a wire bonding option. An aluminum holder was constructed to hold the heater while the TFTC wires were positioned on and epoxied to the TFTC pads. The opposite ends of the nickel and copper TFTC wires were both soldered to copper lead wires to form the reference junction. An ice point dry-well maintained the reference junction temperature at $0^{o}C$.

Before the heater was placed into the experiment, each TFTC was

calibrated in a FC-70 constant-temperature bath. FC-70, with a boiling

temperature of 215°C, allowed calibration up to higher temperatures than

FC-72 (56°C boiling temperature) would allow. The temperature of the

bath was measured with a precision platinum resistance thermometer

probe and displayed on a thermometer readout. The TFTCs were

calibrated over a temperature range of 10°C to 80°C, with a

measurement taken every 5°C. Voltage measurements for a few sample

TFTCs were taken multiple times at each calibration temperature over a

several day time period, always resulting in very repeatable results. Figure

9 shows the calibration curves of three different copper-nickel TFTCs and a

bulk wire copper-nickel thermocouple. The slope of the TFTC calibration

curves, 0.11 ± 0.01 mV/5°C, corresponds consistently to the known

copper-nickel temperature coefficient of 22 μV/^{o}C. These calibration

curves were used to convert thermocouple voltages recorded during the

experiment to surface temperature measurements under the bubbles. A

MATLAB program performed a linear interpolation between each

calibration point to generate a temperature trace from each set of

voltage data.
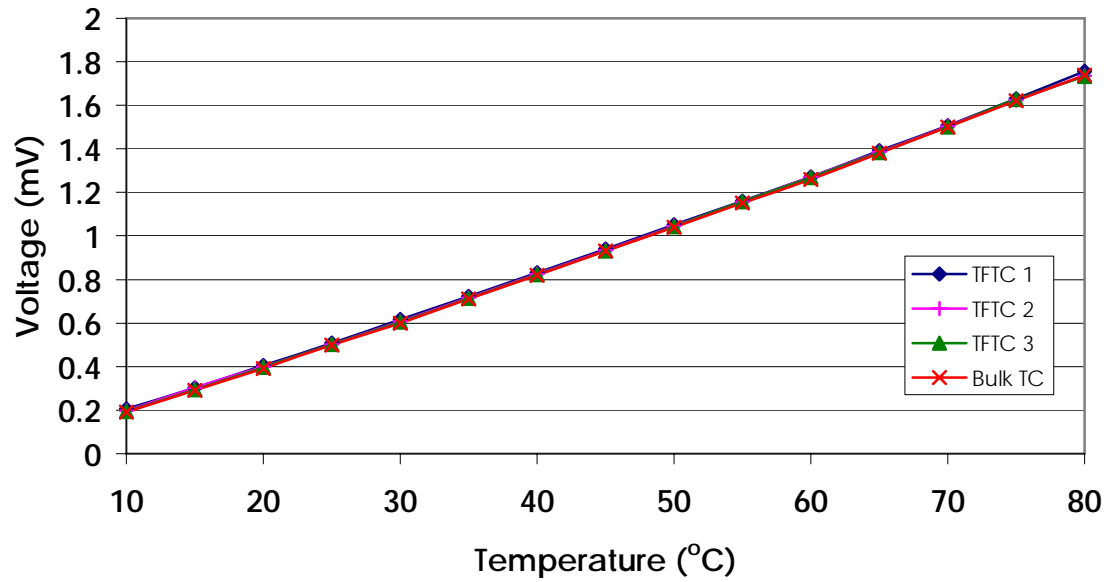
Figure 9: Calibration Curves

<u>Experiment</u>

Test Chamber Setup

A diagram of the experiment setup used for this pool boiling study can be seen in Figure 10. The heater was mounted on a pyramid-shaped platform in a transparent acrylic chamber. An opening was constructed

at the top of the pyramid to create a 1 cm by 1 cm viewing area under the heated portion of the heater while pool boiling occurred on the top surface of the heater.
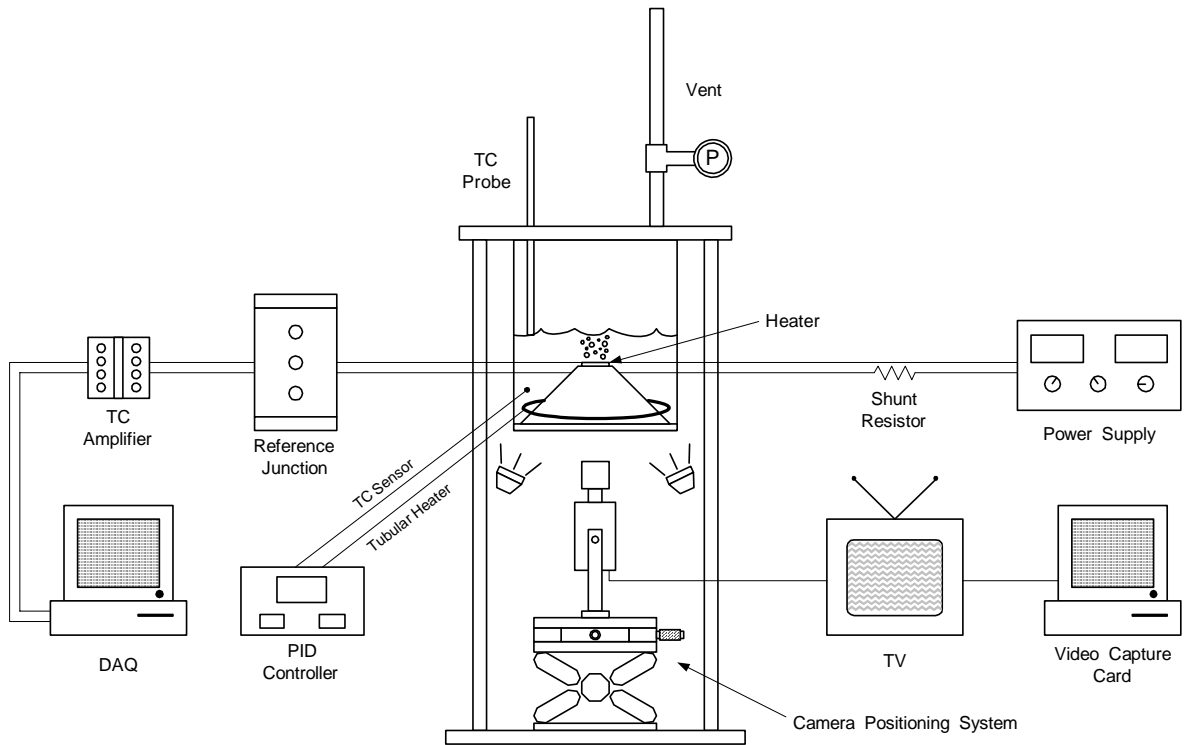
Figure 10: Diagram of Experiment Setup

The TFTC and power wires were run out of the chamber through sealed tube fittings and the chamber was entirely sealed with 100% silicone sealant to prevent FC-72 leakage. The heater was submerged in a FC-72 pool about 3 cm beneath the liquid surface. A tubular heater surrounding the base of the pyramid heated the FC-72 to a saturation temperature of

56°C and was regulated by a T-type thermocouple in the liquid pool that was connected to a PID temperature controller. An additional relay was used to minimize the noise introduced into the experiment by this secondary heater.

An open vent at the top of the chamber maintained the experiment at atmospheric pressure, which was verified with a pressure gage attached to the vent. This vent, made from a long copper tube, allowed FC-72 vapor to condense back into the liquid pool. Dissolved gases also escaped through this vent during degassing. A thermocouple probe monitored the temperature of the liquid-vapor interface to ensure that the dissolved gas concentration was sufficiently low. This procedure is detailed in the degassing section below. An aluminum plate covering the chamber provided a surface for the FC-72 to condense on during boiling. Minimal FC-72 vapor was lost during boiling due to the presence of the vent tube and condenser plate. Design drawings of these various chamber components are located in Appendix A. Photographs of the experiment can be viewed in Appendix B.

Degassing Process

The FC-72 in the chamber was subjected to boiling prior to the experiment in order to remove dissolved gases from the fluid. After the secondary heater raised the temperature of the FC-72 to saturation at 56°C, vigorous boiling at about 10 W/cm² was initiated on the heater. This level of boiling was maintained for at least 30 minutes to allow the dissolved gases to escape from the vent. The temperature at the liquid-vapor interface in the chamber was measured by a T-type thermocouple probe, as seen in Figure 10. This vapor temperature was measured to be 55.5°C ± 0.3°C. The vapor pressure was then calculated using Equation 1, the pressure-temperature relationship for FC-72 established by 3M.

$$T(K) = \frac{1562}{9.729 - \log P(Pa)} \tag{1}$$

This partial vapor pressure was calculated to be 94.2 kPa ± 1 kPa. Using the following relationship between partial gas and vapor pressures and the total pressure in Equation 2, the partial gas pressure can be calculated to be 6.9 kPa ± 1 kPa.

$$P_v + P_g = P_T \qquad\qquad (2)$$

The total pressure in this experiment is known to be atmospheric pressure, 101.1 kPa. Equation 3 shows that the remaining gas content in the liquid, C_g, can be calculated by multiplying the partial gas pressure by Henry's constant, H. Henry's constant for FC-72 was established by You et al. [13] to be 5.4×10^{-5} moles/mole-kPa.

$$C_g = H \times P_g \qquad\qquad (3)$$

The resulting dissolved gas concentration in this study was C_g = 0.00037 moles/mole ± 0.00005 moles/mole. You et al. [13] reported that a gas content of less than 0.0025 moles/mole would have a negligible effect on nucleate boiling.

Experiment Setup

Power was supplied to the heater with a 1000 W (maximum) DC power supply. The voltage was monitored by a digital multimeter. The current

was calculated from the voltage measured across a low-resistance shunt resistor, R = 0.0046307 Ω, also monitored by a digital multimeter.

A programmable gain amplifier amplified the voltages produced by the TFTCs by a factor of 1000. This produced large enough voltage values to be processed by the data acquisition system. Two of these dual instrumentation amplifiers allowed four TFTCs to be monitored simultaneously. After connecting at the amplifiers, the TFTC lead wires entered a shielded connector box, selected to help minimize any noise present in the TFTC signal due to equipment and room effects. A 200 kHz National Instruments data acquisition card along with a LabVIEW program recorded the TFTC voltages. Four channels were used, one for each of the four TFTCs, and each channel was sampled at 50 kHz for one second. LabVIEW software was also used to digitally filter the voltages to reduce some of the noise components in the signal. A low pass filter with a 1000 Hz cutoff frequency and two band stop filters with 60 Hz and 120 Hz cutoff frequencies were used.

A high-speed CCD camera was mounted below the heater to observe the bubbles growing on the top surface of the heater. The camera was attached to a translation stage, whose precision micrometers allowed the

camera position to be horizontally adjusted so that the entire heated

surface could be scanned. The translation stage was mounted to a lab

jack so that the vertical position of the camera could be adjusted.

Varying lengths of camera extension tubes altered the magnification of

the heater surface. Bubble images were recorded on the camera

control/display unit at 2000, 4000, and 8000 frames per second. The

bubble images were transferred to a VCR tape so they could be viewed

on a larger television screen at slower frame rates. The images were also

examined frame-by-frame with a video capture card in a personal

computer. The bubble images were viewed and measured from the

television screen with the TFTC width serving as the reference length.

Using the known TFTC width of 50 μm, the relative bubble sizes could be

calculated.   A trigger incorporated into the LabVIEW program allowed

the bubble images from the camera to be synchronized with the TFTC

voltages from the heater.

Experiment Procedure

After the liquid pool was heated to the 56°C saturation temperature and

the FC-72 was thoroughly degassed, the experiment was performed and

information was recorded. Data from four heaters was obtained in this pool boiling experiment; two with fused silica insulation layers called FS-1 and FS-2, and two with sapphire insulation layers called SP-1 and SP-2.

The input power, P, to the heater was determined from the standard power relationship in Equation 4, where the voltage, V, was the value set on the power supply and the current, I, was calculated across the shunt resistor.

$$P = I \times V \tag{4}$$

The input heat flux was determined from the input power by the method described in the following uncertainty section.

Once boiling was occurring at the desired input heat flux, the high-speed camera was positioned below the heater to observe the location of interest on the heater surface. These locations were typically either one of the TFTC junctions or a specific active cavity. The camera then began recording the bubble images at 2000 frames/second. The DAQ LabVIEW program was then initiated, recording one second of data, or 50000 voltage measurements, for each of the four channels. The program

simultaneously sent a trigger to the camera to stop recording, thereby storing the previous two seconds of images into the camera buffer. The voltage data was filtered to reduce noise in the output signal, and a power spectral density function was also applied to monitor the frequency of temperature fluctuations. Comparing these frequencies to the known frequencies of the noise fluctuations allowed the temperature drops to be distinguished from the noise.

The MATLAB program converted the filtered voltage values to temperature values by interpolation of the amplified calibration curves. The 2000 images in the final second of bubble images stored in the camera buffer could then be correlated to the 50000 temperature readings taken in the one second from each TFTC. There were 25 temperature measurements corresponding to each camera frame, or 25 temperature measurements per 0.5 ms.

The bubble images were transferred to VCR tapes with a camcorder and were observed on a television screen. Measurements of the TFTC width, bubble diameter, contact ring diameter, and field-of-view size were made from the screen with a digital caliper and a ruler. Bubble lifetime and growth rate were observed by counting the number of frames, where

each frame represented 0.5 ms. The VCR allowed the images to be examined frame-by-frame to make size and time measurements possible and a video capture card allowed individual bubble images to be extracted and analyzed.

Uncertainty Analysis

Not all of the power supplied to the ITO was concentrated between the two power pads in the central 1 cm by 1 cm area of interest; some of the power was conducted to the outer areas of the heater. An analysis of the current flow, detailed in the following section, established that approximately 70% of the input power was conducted through the center area of the heater. At a low heat flux of 1 W/cm^2, the uncertainty was $\pm$ 0.02 W/cm^2. At a higher heat flux of 6 W/cm^2, the uncertainty was $\pm$ 0.12 W/cm^2.

The uncertainty in the temperature values measured by the TFTCs had many sources. The platinum resistance thermometer used during calibration ($\pm$ 0.018^{o}C), the reference junction dry-well ($\pm$ 0.02^{o}C), the DAQ resolution ($\pm$ 0.11^{o}C), noise in the voltage signal ($\pm$ 0.2 ^{o}C), and

interpolation from the calibration curve (± 0.1°C) all contributed. The total

uncertainty in the absolute TFTC temperature values was calculated to be

less than ± 0.5°C and in the temperature fluctuations was less than ± 0.2°C.

The uncertainty in the TFTC width was measured by the optical

profilometer to be 50 μm ± 0.5 μm. This uncertainty, combined with the

uncertainty in the measurement of the TFTC width from the television

screen, typically ± 1 mm, resulted in a total uncertainty in the bubble

measurement of ± 10%. Therefore, for a bubble diameter of 500 μm, the

uncertainty in the measurement was ± 50 μm, and for a bubble diameter

of 1000 μm, the uncertainty was ± 100 μm.

Current Flow Analysis

Power was supplied to the heater by current conducted through the ITO

from an aluminum power pad on one end of the heater to a power pad

on the opposite end, as seen in Figure 4. These 10 mm wide power pads

were centered on each end of the 17 mm wide heater, and it was this 10

mm wide area between the two power pads that needed to be heated

for this experiment. It was apparent, though, that not all of the current

was conducted directly from one power pad to the other; some of the current leaked into the 3.5 mm wide space on each side of this central area. Therefore, the heat provided to the central 10 mm by 12 mm area of the heater was less than the overall heat input to the heater.

An analysis of this current leakage provided an estimate of the actual heat flux supplied to the central area of interest on the heater. The 17 mm wide ITO layer was divided into seventeen 1 mm wide sections, as seen in Figure 11 below. The approximate distance the current would have to travel from one power pad to the other for the eleven sections directly between the power pads, sections 4 through 14, was 12 mm. The three outer sections on each side of the central area were estimated to be 14 mm, 16 mm, and 18 mm long for sections 3 and 15, 2 and 16, and 1 and 17, respectively. Based on the definition of resistance, R, as a function of the material resistivity, ρ, shown in Equation 5, the resistance of each ITO section was directly proportional to this length, L.

$$R = \frac{\rho \times L}{A} = \frac{\rho \times L}{t \times 1mm} \Rightarrow R \propto L \qquad (5)$$
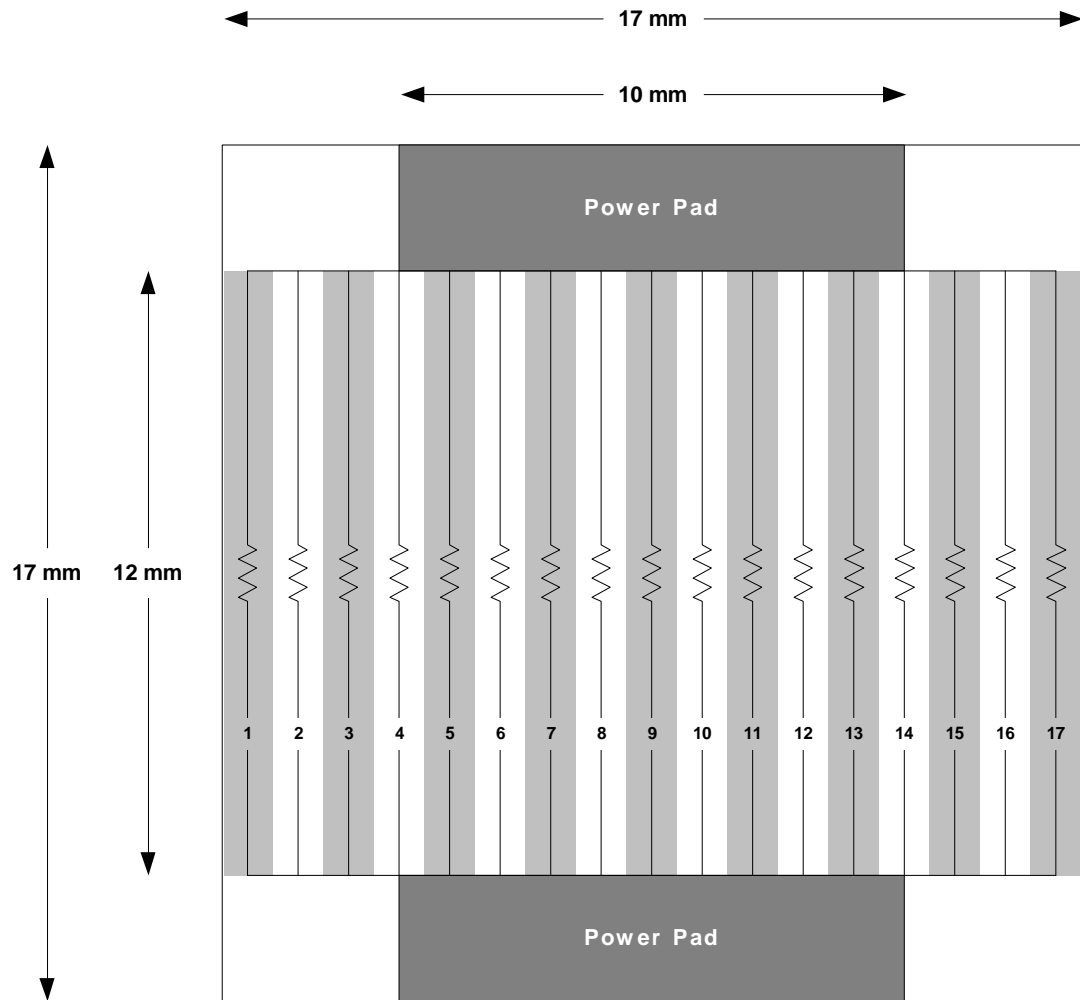
Figure 11: Current Analysis

For a constant voltage applied across the heater, and therefore across each section, the power to each section, P, was inversely proportional to this length, L, as shown in Equation 6.

$$P = \frac{V^2}{R} \propto \frac{1}{L} \tag{6}$$

Therefore, for the inner eleven sections, the power was proportional to

1/12 mm, or 0.083. For the outer sections, the power was proportional to

1/14 mm, 1/16 mm, and 1/18 mm, or 0.071, 0.063, and 0.056, respectively.

For the inner sections 4 through 14, 0.083 multiplied by 11 gives 0.913, the

representative power through the central eleven sections of the heater.

Multiplying 0.071, 0.063, and 0.056 each by 2 gives the representative

power through the six outer sections; 0.142 for sections 3 and 15, 0.126 for

sections 2 and 16, and 0.112 for sections 1 and 17. The total

representative power can be calculated by adding these four numbers,

0.913, 0.142, 0.126, and 0.112 together to equal 1.293. Dividing 0.913, the

representative power through the center of the heater, by 1.293, the total

representative power to the heater, equals 0.7, the estimated portion of

the total power conducted through the central area of the heater.

So from this analysis it was calculated that approximately 70% of the input

power was supplied to the inner eleven sections of the heater; the

remaining 30% was to the outer six sections. Therefore, a reduction factor

of 0.7 could be applied to the input power value to calculate the power

supplied to the central area of the heater. This reduced power value,

divided by the 10 mm by 12 mm area in question, established the heat

flux for the central area of interest.

Similar analyses involving the current traveling by slightly shorter or longer

paths through the outer six sections of the heater result in similar reduction

factors.

<u>Data Resolution</u>

Rini et al. [3] reported that FC-72 pool boiling bubbles at low heat fluxes

had an 8-10 ms bubble lifetime and a 400-500 μm bubble departure

diameter. It was important to confirm that the spatial resolution, temporal

resolution, and camera frame rate chosen for this study were sufficient to

capture the details of the bubble behavior and surface temperatures that

occurred in this experiment. The TFTC junction size was 25 μm by 25 μm,

significantly smaller than the bubble departure diameter and therefore

able to capture localized temperature fluctuations during bubble growth.

The 50 kHz sampling rate for each TFTC recorded 50 temperature values

for each millisecond of the 8-10 ms bubble lifetime. In addition, the

thermal response time of the TFTC was known to be less than 1 μs [14, 15]. These values ensured that no details of the temperature fluctuations could be overlooked. The camera simultaneously recorded 2 frames for every millisecond of the bubble lifetime at a 2000 frames per second frame rate, allowing the bubble and contact ring growth rates to be observed.

With four TFTCs, each only 50 μm wide, only a small percentage of the heater surface was obscured by the TFTCs. This condition, combined with the transparent heater layers, allowed the entire heater surface to be observed. Camera images recorded during bubble growth were approximately 1mm by 1mm in size, larger than the typical bubble departure diameter. Consequently, individual bubbles could be observed in their entirety on the screen and all stages of their growth and departure could be monitored. At times the camera magnification was reduced to view a larger area of the heater surface so that multiple TFTCs and bubble interaction could be observed.

RESULTS

Bubble Images

The following photographs are sample images of the boiling surface of the heater taken from below the heater. These images were recorded with the high-speed camera at a frame rate of 2000 frames/second. The vertical line in the center of Figure 12 is the 50 μm wide TFTC. The slight offset in the TFTC line near the center of the image is where the copper and nickel films overlap to form the 25 μm by 25 μm TFTC junction, indicated in the figure.
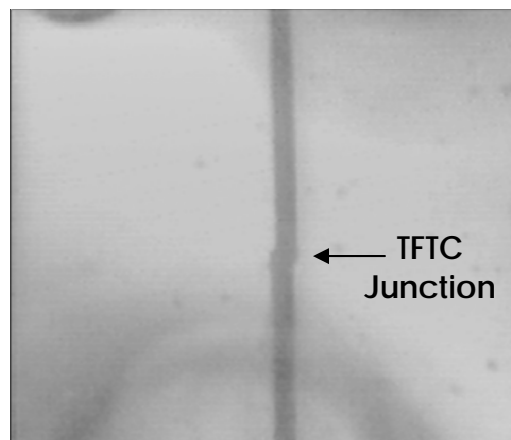

Figure 12: Image of TFTC

Figures 13 through 16 display different types of bubble images observed during the course of this experiment. Figure 13 shows a bubble growing directly over the TFTC junction while Figure 14 shows a bubble growing from a cavity near the TFTC junction. The process of two individual bubbles merging to form a larger bubble can be seen in Figure 15. A photograph of the heater populated with multiple bubbles is shown in Figure 16, which was recorded during subcooled boiling where bubbles were typically smaller and more numerous.
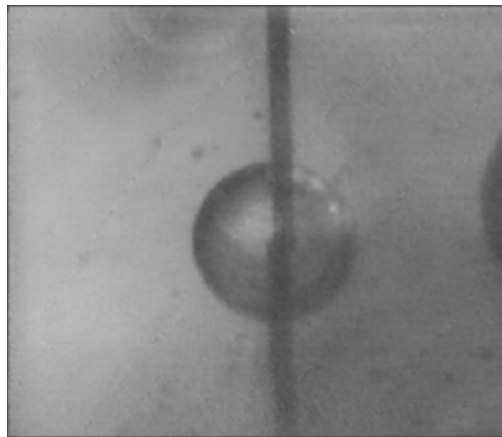

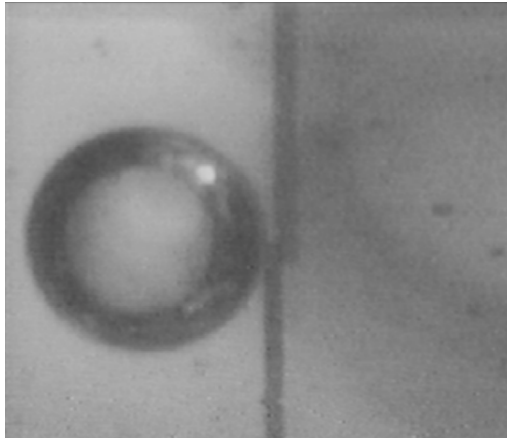**Figure 13: Image of Bubble Over the TFTC Junction**

Figure 14: Image of Bubble Near the TFTC Junction

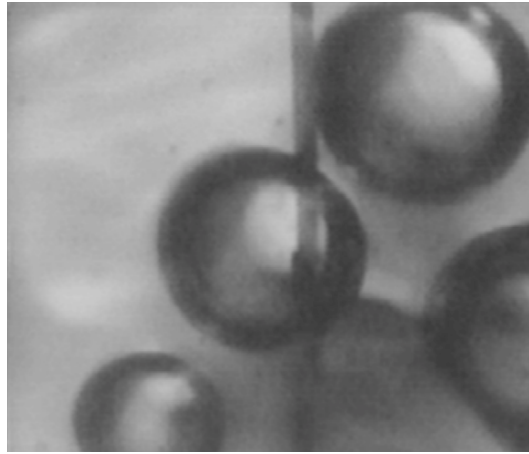**Figure 15: Image of Merging Bubbles**

Figure 16: Image of Multiple Bubbles

Figure 17 illustrates a bubble characteristic called the contact ring that is repeatedly observed in the bubble images. The picture on the left shows a typical bubble at an intermediate stage of its growth. The outer circle and inner circle, superimposed on the picture of the same bubble on the right, represent the outer liquid-vapor interface of the bubble surface and the contact ring, respectively. The contact ring is the vapor-liquid-solid line where the vapor enclosed in the bubble, the liquid surrounding the bubble, and the solid wall all intersect. The light-colored space within the contact ring is the dry area under the bubble. The dark-colored space between the inner and outer circles is the area below the vapor bubble where the surface is still wet and the microlayer has formed. The outer circle represents the actual bubble diameter.
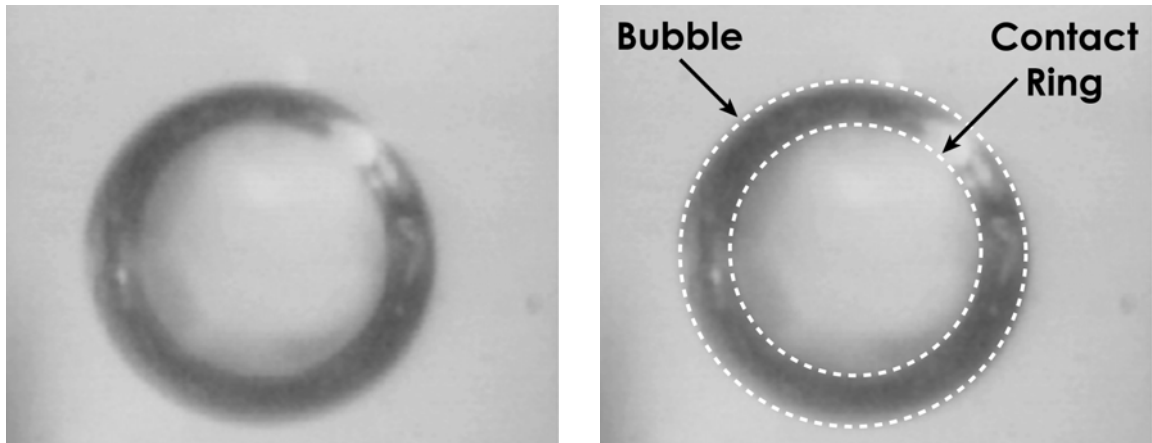
Figure 17: Bubble and Contact Ring

A growth cycle of a pool boiling bubble with a 7 ms lifetime is depicted in Figure 18, where each frame represents 0.5 ms of the bubble lifetime. This bubble growth cycle, recorded at 3 W/cm² from the fused silica FS-2 heater, corresponds to the side view of the growth cycle sketched in Figure 1. The waiting period can be observed in Frame 1, where no bubble was present. In Frame 2, the bubble has emerged from the cavity and has started to grow. Frame 3 shows that most of the area under the bubble was dry; the microlayer in that region had already evaporated. By Frame 5 the contact ring had reached its maximum size and the entire microlayer had evaporated. As the bubble began to depart in Frame 6, the contact ring began to shrink, and liquid rewet the surface that was previously dry under the bubble. At Frame 14 the contact ring had almost disappeared, signaling that bubble departure was imminent.
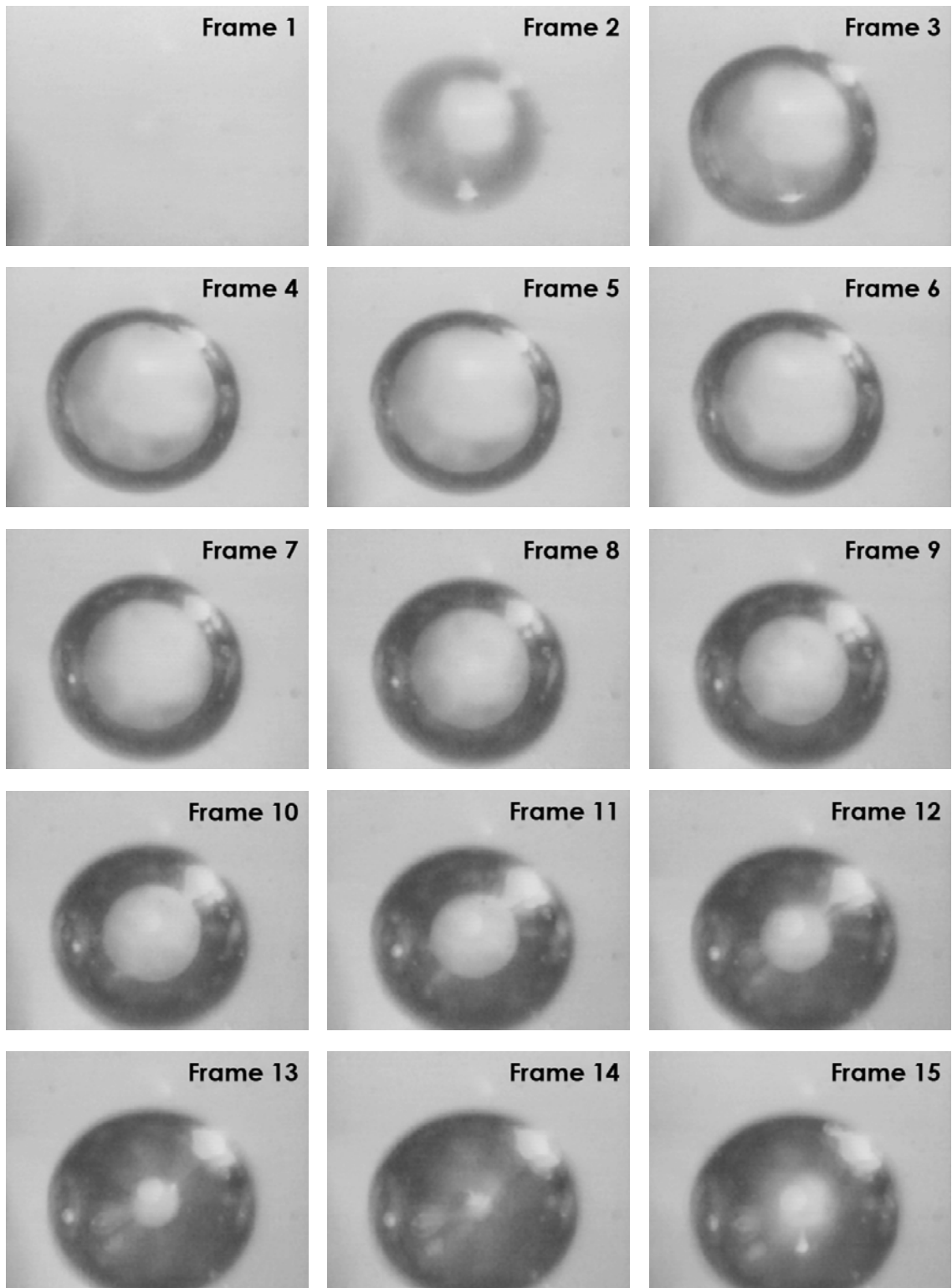
Figure 18: Bubble Growth Cycle with 0.5 ms time step (FS-2 heater)

In Frame 15 the bubble had completely departed from the surface. The light-colored area viewed in the center of the bubble was due solely to a reflection of the light source.

Temperature Data

The DAQ recorded 50,000 TFTC voltages over one second for each of the four TFTCs. A sample of a temperature trace for one TFTC on the fused silica FS-1 heater, taken at approximately 1 W/cm^2, is shown in Figure 19.
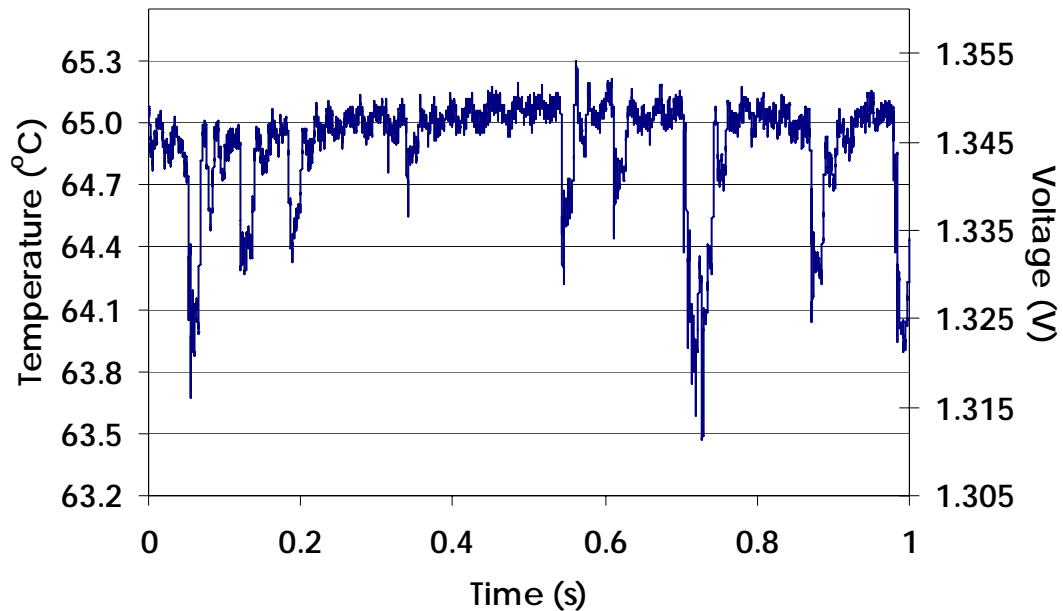

Figure 19: Temperature Trace of TFTC at 1 W/cm^2 (FS-1 heater)

A typical temperature seen here is 65°C, which corresponds to about 1.346 V. This temperature-voltage relationship was determined from interpolating the data in the calibration curve. A voltage change of 0.022 V corresponds to a 1°C temperature change, so the largest temperature drop in this trace is approximately 1.5°C. By comparison, temperature fluctuations in Figure 19 due to noise in the TFTC signal seen were on the order of ± 0.1°C. From observing the simultaneous bubble images, it was confirmed that these 1-2°C temperature drops occurred when a bubble grew or departed over the TFTC junction. Each of these temperature drops observed in Figure 19 was actually composed of multiple temperature fluctuations, due to either a single bubble or consecutive bubbles. It is evident from counting the number of regions where the temperature dropped that nine periods of bubble activity occurred over the TFTC junction in this one-second time period. The magnitude of these temperature drops at a constant heat flux was affected by the location of the nucleation site relative to the TFTC junction, the bubble growth rate, and the location and growth pattern of the contact rings.

<u>Bubble and Temperature Correlation</u>

Fused Silica Heater

When a bubble grew out over a TFTC junction from a cavity near the junction, its contact ring enlarged and crossed over the junction. As the bubble began to depart, the contact ring grew smaller and crossed over the junction again. Both of these events were accompanied by temperature drops. A set of these temperature drops for three periods of bubble activity, and the synchronized bubble images, are displayed in Figures 20, 21, and 22. This data was recorded at approximately 1 W/cm^2 input heat flux, all from the first of two heaters with fused silica insulation layers tested in this experiment, heater FS-1. The bubble images in all three of these figures cover about a 1 mm by 1 mm area of the heater surface. The vertical line in the pictures is one TFTC, and the slight offset in the line indicated by an arrow in each image is the TFTC junction formed where the copper and nickel films overlap. The bubbles in these images emerged from a nucleation site located just below the TFTC junction. The darker shadows seen in the background are bubbles that have already departed from an adjacent nucleation site. These images were taken at

2000 frames/second, so there are 25 TFTC temperature measurements corresponding to every frame. The shaded areas and their correlated bubble images represent the 25 temperature values in the shaded region.
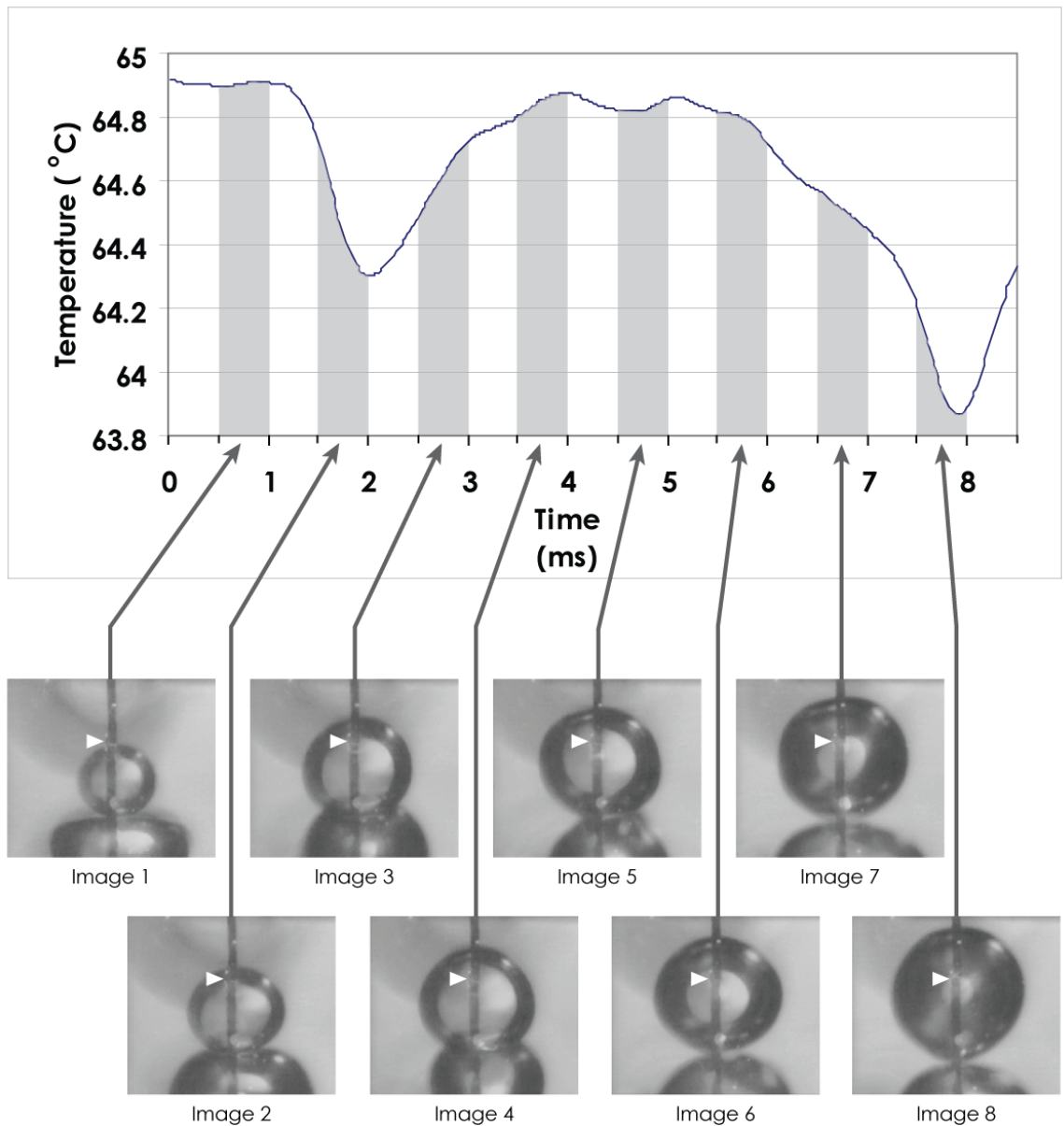

Figure 20: First Temperature and Bubble Correlation (FS-1 heater)

In Figure 20 above, the growth of a single bubble over the TFTC junction is observed. This bubble had an 8.5 ms lifetime; therefore 17 frames exist between bubble emergence and bubble departure. Time on the temperature trace is divided into 0.5 ms increments, so there is one frame corresponding to every time increment. Eight of these 17 frames are correlated to the surface temperature of the TFTC, illustrated by the eight shaded areas in the graph. The second image and the seventh image demonstrate the contact ring crossing over the TFTC junction during bubble growth and departure, respectively. It is apparent that the surface temperature drops are related to this movement of the contact ring. The first temperature drop that occurred while the contact ring was crossing the TFTC junction during bubble growth was about $0.6^{o}C$ and took place over less than 1ms.   The second temperature drop, due to the contact ring crossing back over the TFTC junction during bubble departure, was about $1^{o}C$ and took place over approximately 2 ms.

Like Figure 20 above, Figures 21 and 22 were recorded at 1 W/cm^2. They also have one frame corresponding to every 0.5 ms time increment, with eight frames displayed in both figures, and 25 temperature measurements plotted for each 0.5 ms time increment, specified by the shaded areas.
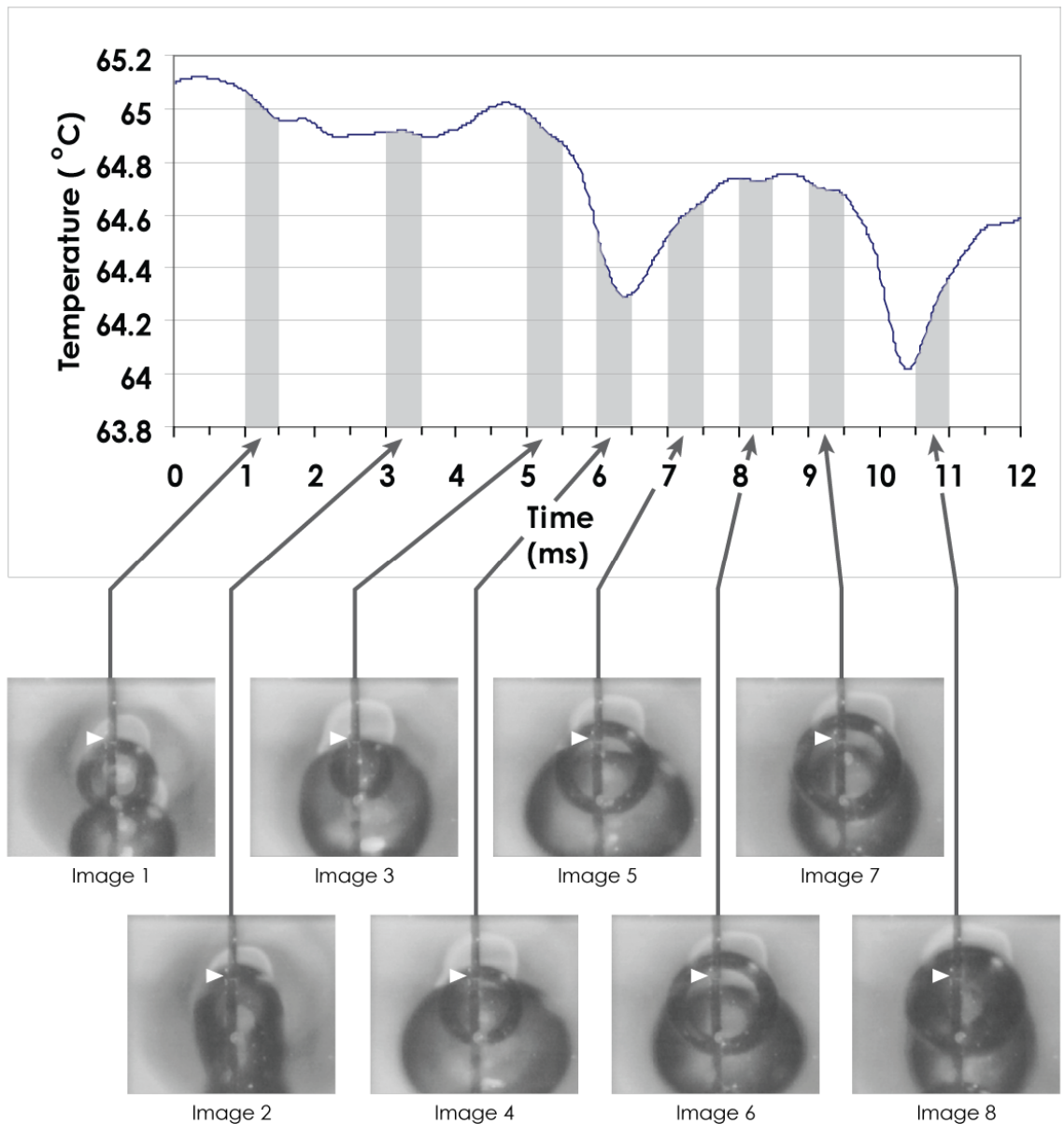
Figure 21: Second Temperature and Bubble Correlation (FS-1 heater)

In the first image of Figure 21, a bubble has emerged from the cavity

below the TFTC junction. After 1.5 ms, the outer edge of the bubble has

crossed the TFTC junction, which is indicated by an arrow. The contact

ring, though, did not cross the junction, and therefore no significant temperature drop occurred. The second image shows the bubble merging with a bubble from an adjacent nucleation site, which then departed. A second bubble emerged from the same cavity, as seen in the third image, and its contact ring did cross the TFTC junction, seen in the fourth image. This caused a temperature drop of approximately $0.6^{\circ}C$ in just over 1 ms. The fifth, sixth, and seventh images show the TFTC junction located at the dry spot under the bubble, corresponding to the temperature increase observed in the temperature trace as the surface reheated. At 9.5 ms the bubble began to depart, and the contact ring crossed the TFTC junction again, causing the temperature to drop about $0.7^{\circ}C$ in approximately 1 ms. In the final image, the cooler bulk liquid has rewet the TFTC junction and the temperature recovery began due to the heating of the liquid. The bubble then departed after an 8 ms lifetime.

Figure 22 displays multiple temperature drops, corresponding to the presence of multiple successive bubbles. The contact ring of the first bubble, shown in the first image, crossed the TFTC junction, producing a temperature drop of approximately $0.6^{\circ}C$ in less than 1 ms. This bubble then merged with a neighboring bubble. A second bubble emerged from the cavity at 4 ms between the first two images, but its contact ring

did not completely cross the TFTC junction, so only a small temperature
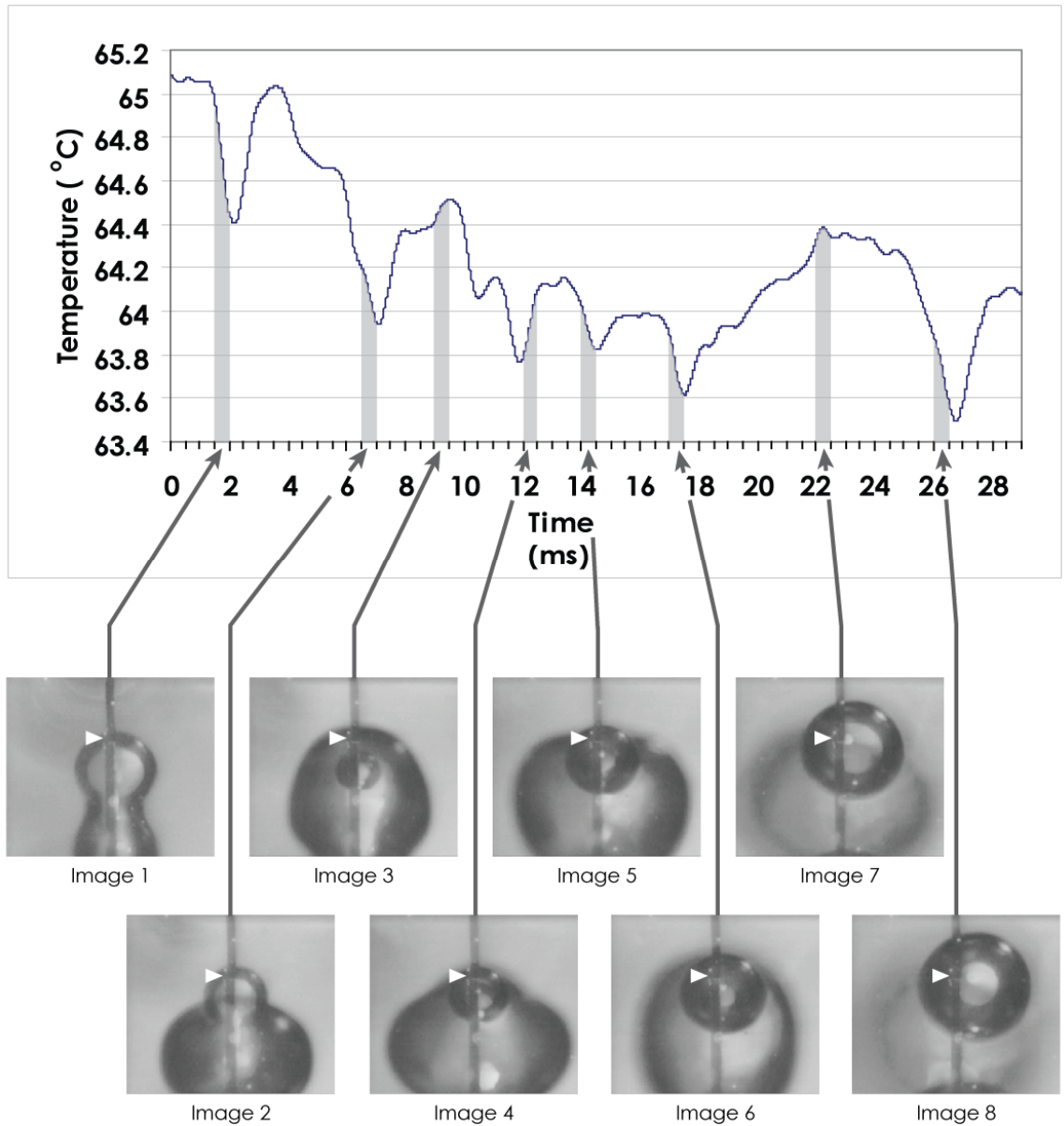
drop occurred.

Figure 22: Third Temperature and Bubble Correlation (FS-1 heater)

A third bubble began to grow, seen in the second image, generating a 0.7°C temperature drop in just over 1 ms when its contact ring crossed the TFTC junction during bubble growth . This bubble also merged with the larger bubble nearby. A fourth bubble appears in the third image; it merged with the nearby bubble before its contact ring crossed the TFTC junction, therefore no temperature drop occurred. Finally, a fifth bubble began to grow at 10 ms and can be first seen in the fourth image. Between 10 ms and 20 ms, four small temperature drops can be observed. This was due to the contact ring repeatedly crossing the TFTC junction while the bubble oscillated on the surface. These oscillations were possibly caused by interaction with the neighboring bubble or by the emergence of small, undetectable vapor bubbles emerging from the cavity and merging with the primary bubble. Finally after 20 ms the oscillations ceased and the bubble increased in size to its departure diameter. The TFTC junction was clearly located at the dry spot under the bubble, shown in the seventh image, corresponding to the temperature increase between 18 ms and 24 ms. The contact ring crossed the TFTC junction one additional time during bubble departure, creating a temperature drop of approximately 0.9°C in over 1.5 ms. This bubble remained on the surface until its departure at 29 ms.

Microlayer Evaporation

The temperature drops observed from a fused silica heater in Figures 20, 21, and 22 above are similar to the temperature drops observed in the previous studies described in the background section ([4], [6], [7], [11]). Careful observation of the synchronized bubble images confirmed that these temperature drops are indeed due to microlayer evaporation during bubble growth and liquid rewetting the heater surface during bubble departure. More specifically, the temperature drops occur when the vapor-liquid-solid contact line crosses the TFTC junction during bubble growth and departure. This demonstrates that microlayer evaporation at the contact line and cooler bulk liquid rewetting the surface at the contact line may locally remove more heat from the surface than other mechanisms under a bubble. But the relatively small magnitude and time duration of these temperature drops, even at higher input heat flux levels, suggests that the heat removed from the surface at this contact line may not be the prevailing heat flux contribution from the heater surface during nucleate boiling. In addition, the similar magnitudes of the two types of temperature drops observed in this experiment, due to microlayer evaporation and liquid rewetting the surface, also support more recent

theories of pool boiling heat transfer [8, 9, 10, 11] rather than the earlier theories of dominant microlayer evaporation [4, 6].

Sapphire Heater

Two heaters with sapphire insulation layers instead of fused silica insulation layers were also tested. The chief differences in these two insulation layers were the thickness and the thermal properties. The sapphire insulation layers had a 0.2 mm thickness and a 15.1 x 10^{-6} m^2/s thermal diffusivity, while the fused silica insulation layers had a 0.1 mm thickness and a 0.834 x 10^{-6} m^2/s thermal diffusivity. Correlations between bubble images and temperature traces for the heaters with sapphire insulation layers, like the correlations for the fused silica heaters, were performed. A sample result of a single bubble growth cycle from the first sapphire heater, SP-1, is shown in Figure 23. This bubble had a lifetime of 16 ms, where each frame corresponded to 0.5 ms and 25 temperature measurements. It is apparent from both the third image and the final image that the contact ring clearly crossed the TFTC junction during bubble growth and bubble departure, yet no observable temperature drops larger than the ± 0.2°C noise fluctuations from the TFTC signal are present in the temperature

results. This lack of temperature drops due to contact line movement was consistently absent from all the sapphire heater results. Further investigation into this occurrence is described in the following section.
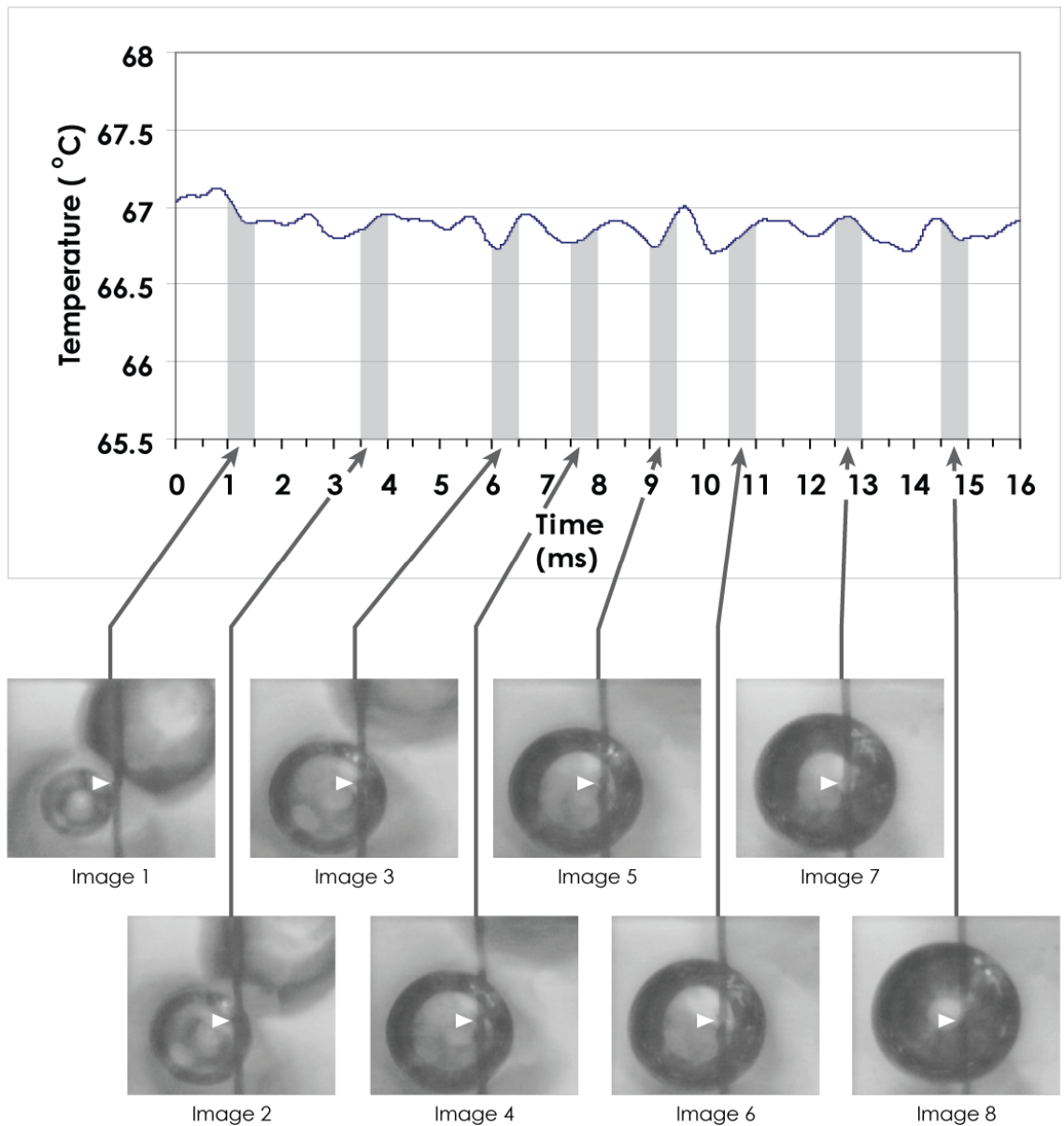

Figure 23: Fourth Temperature and Bubble Correlation (SP-1 heater)

Heater Simulation

Guo and El-Genk [16] developed a numerical model of microlayer evaporation from a heated surface during nucleate boiling. This model calculated the change in wall temperature over time due to microlayer evaporation at the contact line. The temperature results were presented from two substrate materials, stainless steel and copper, where copper has up to a 30 times larger thermal diffusivity than stainless steel. For the stainless steel heater, the temperature dropped to about 50% of its initial value over a few milliseconds. For the copper heater, the temperature dropped to only about 90% of its initial value over a few milliseconds. Therefore the heater with the significantly larger thermal diffusivity experienced a considerably smaller temperature drop. These findings were concluded to be a direct consequence of the increased lateral heat conduction that occurs in substrates with higher thermal diffusivities. This study had also examined the effect of substrate wall thickness on the temperature drop; a thicker wall also increased lateral heat conduction, and therefore a smaller temperature drop occurred during microlayer evaporation, when compared to a thinner wall.

Based on these results, it was apparent that a heater with a thicker wall and higher thermal diffusivity would have smaller temperature drops produced by bubble growth and departure. In this experiment, the sapphire heaters had insulation layers twice as thick and with a thermal diffusivity 18 times larger than the fused silica heaters, and therefore would be expected to have smaller temperature drops. The lack of observable temperature drops in the sapphire heater experimental data from this study was supported by these numerical results.

Simulations of the fused silica and sapphire heater were developed to confirm why the temperature drops observed in the fused silica heater data were missing from the sapphire heater data. COMSOL Multiphysics, a finite element analysis software, was used to create two-dimensional simulations that approximated the growth of a typical bubble over the TFTC junction. The side view modeled sections for both fused silica and sapphire heaters were 400 μm long and can be viewed in Figure 24. The only differences in the two models were the thickness, 0.1 mm for the fused silica heater and 0.2 mm for the sapphire heater as in the experiment, and the thermal properties of the layers, indicated in Figure 24. Both edges of the modeled section had thermal insulation boundary

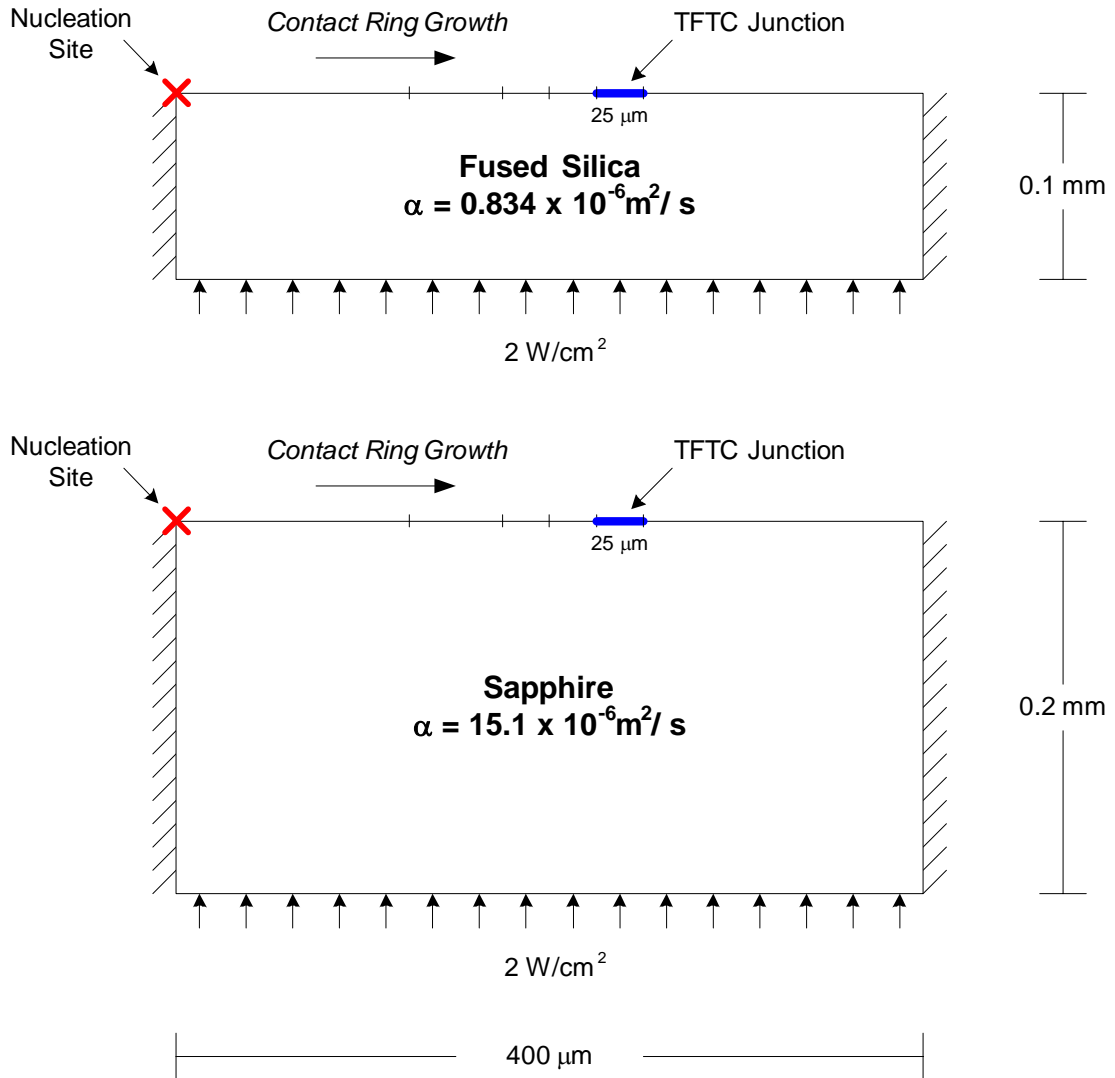conditions, and a typical heat source of 2 W/cm² was applied to the

bottom of the layers.

Figure 24: Fused Silica and Sapphire Simulation Models

Using a surface temperature result from the experimental data, a surface superheat of 10°C was assumed. Substituting the input heat flux, q'', and surface superheat, ΔT, into Equation 7, the average heat transfer coefficient, h, at the top surface of the heater was estimated to be 2000 W/m²-K.

$$q'' = h\Delta T \tag{7}$$

A steady-state simulation with these four boundary conditions was initially performed to establish a temperature field within the section.   A bubble was then assumed to emerge from a cavity at the left corner of the model. The simulated contact ring moved to the right across the surface with a width and simulation time period chosen to facilitate the execution of the simulation and presentation of results, although the combination of these chosen width and simulation time values accurately reflected the diameter and growth rate of an actual bubble. The part of the surface under a dry spot after being passed by the contact ring was assumed to have a low heat transfer coefficient of 10 W/m²-K. Areas of the surface not yet covered by the contact ring retained the initial heat transfer coefficient of 2000 W/m²-K. For the fused silica heater simulation, the value of the heat transfer coefficient associated with high heat removal

at the contact ring was chosen by trial and error. The goal was for the

surface temperature behavior at the simulated TFTC junction to match the

temperature drops observed in the experiment when the contact ring

crossed the TFTC junction. A contact ring heat transfer coefficient of

18000 W/m^2-K accomplished this. Figure 25 shows the result from the final

simulation period of the side view fused silica heater model when the
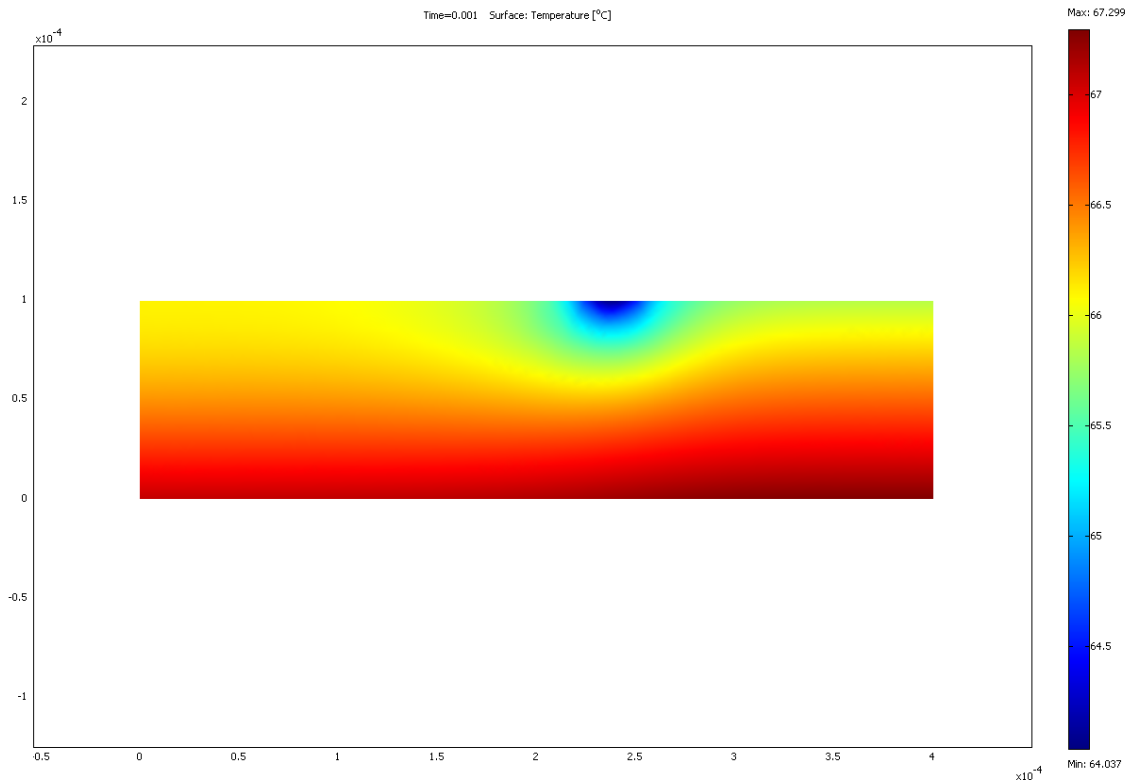
contact ring has crossed the TFTC junction.

Figure 25: Fused Silica Heater Simulation Result

(Units: meters for left and bottom axes, ^{o}C for right axis)

Figure 26 shows the temperature drop that occurred at the junction to be 1.4°C in 1 ms. This temperature drop corresponds to the maximum typical experimental temperature drop observed in the fused silica heater at this heat flux. This combination of contact ring width and heat transfer coefficient was chosen to achieve the desired temperature drop.
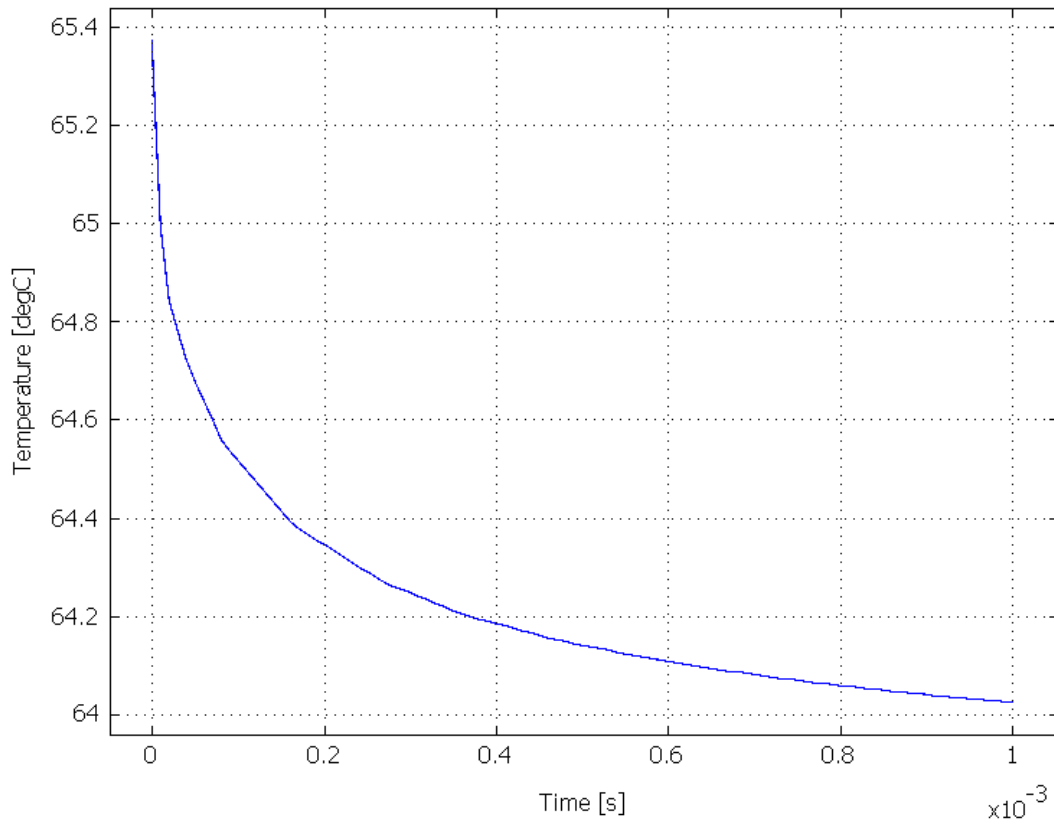

Figure 26: Fused Silica Heater Temperature Simulation Result

Once these values were established for the fused silica heater, the same bubble growth rate and contact ring, dry spot, and average surface heat transfer coefficients were applied to the sapphire heater model. Figure 27 shows the result from the final simulation time period where the simulated contact ring has crossed the TFTC junction.
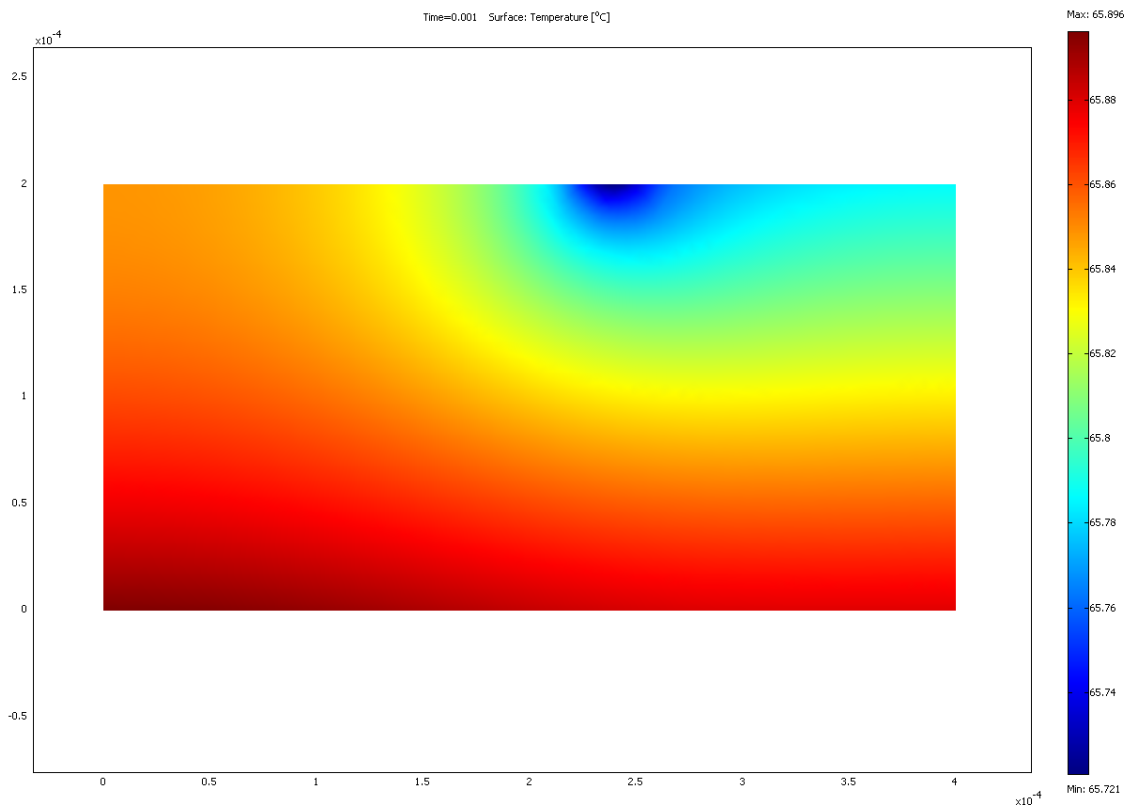

Figure 27: Sapphire Heater Simulation Result

(Units: meters for left and bottom axes, ᵒC for right axis)

The subsequent temperature drop, seen in Figure 28, is only 0.04°C in 1 ms, significantly less than the corresponding 1.4°C resulting from the fused silica heater simulation. These simulation results explain the absence of measurable temperature drops in the sapphire experimental results and also support the previous observations that thicker heaters with higher thermal diffusivities experience greater lateral heat conduction and therefore smaller temperature drops due to nucleate boiling [16].
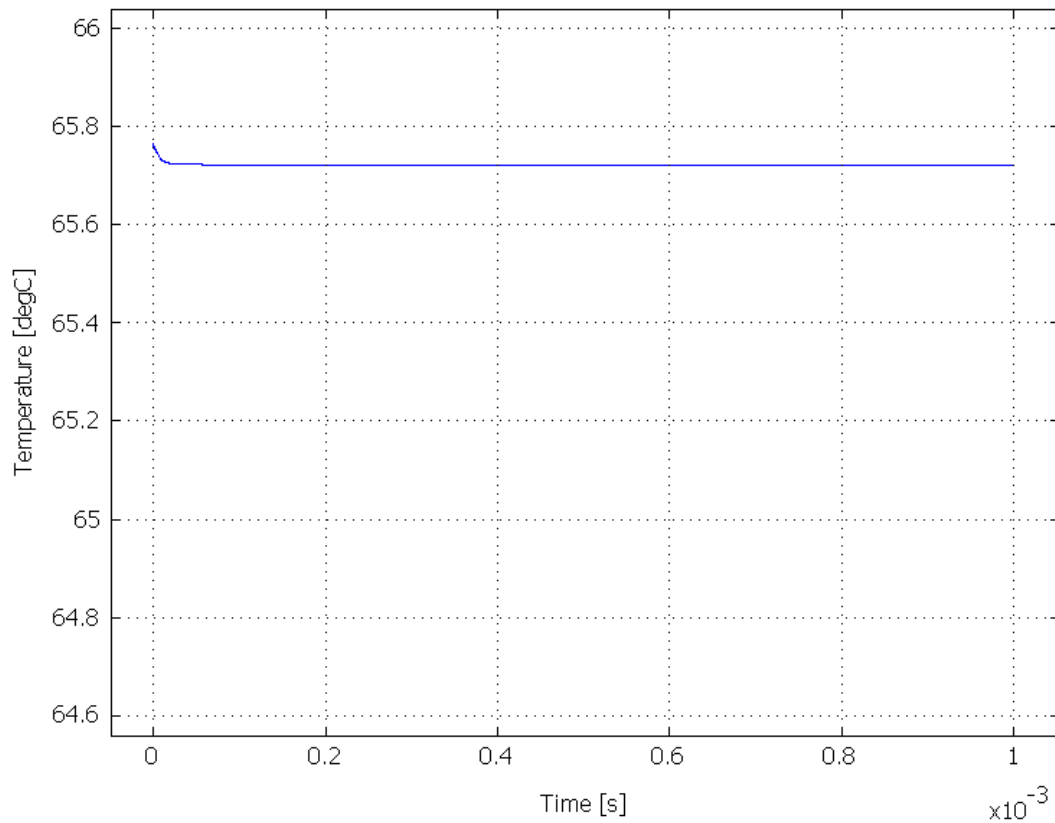

Figure 28: Sapphire Heater Temperature Simulation Result

A second simulation of the sapphire heater with a thickness equal to the fused silica heater thickness yielded a similarly small temperature drop; therefore in this experiment only the thermal properties of the substrate were a limiting factor in the surface temperature fluctuations.

The temperature distribution results for each time step for both the fused silica and sapphire heater simulations are located in Appendix C.

<div align="center">Nucleate Boiling Contribution</div>

Heat is removed from the surface of the heater by both nucleate boiling and enhanced convection heat transfer. The contribution to the total heat removal by liquid-to-vapor phase change during bubble nucleation can be calculated using Equation 8, where h_{fg} is the latent heat of vaporization, ρ_v is the vapor density, V_b is the bubble volume, f is the bubble departure frequency, and n is the bubble site density.

$$q'' = h_{fg} \times \rho_v \times V_b \times f \times n \qquad (8)$$

The values of h_{fg} and ρ_v for FC-72 are known to be approximately 88 kJ/kg

and approximately 14 kg/m³, respectively.   Assuming a spherical shape

for the bubble, the bubble volume was estimated using Equation 9, where

d_d is the bubble departure diameter.

$$V_b = \frac{4}{3}\pi\left(\frac{d_d}{2}\right)^3 \tag{9}$$

This analysis of the nucleate boiling contribution to the total heat transfer

was performed at three different input heat fluxes, 1 W/cm², 1.75 W/cm²,

and 2.9 W/cm², using data from the FS-1 fused silica heater tested in this

experiment. The bubble volume was calculated with a typical bubble

departure diameter value of 600 μm, measured from the recorded

bubble images. The bubble frequency was determined by averaging the

number of bubbles departing from a cavity during one second at four

different cavities. The bubble site density was established by counting the

number of active sites on the heater while scanning the entire surface

with the high-speed camera.

At 1 W/cm², the bubble departure frequency and bubble site density

were observed to be 30 bubbles/s and 25 sites/cm², respectively. Using

Equation 8, the heat flux from the surface due to bubble vapor generation was calculated to be 0.1 W/cm^2. Therefore, the contribution of nucleate boiling to the overall heat transfer from the surface at an input heat flux of 1 W/cm^2 was approximately 10%.

These calculations were repeated for 1.75 W/cm^2 and 2.9 W/cm^2, where nucleate boiling contributed approximately 23% of the heat removed from the surface at 1.75 W/cm^2 and approximately 35% at 2.9 W/cm^2. The data and results for all three heat fluxes are listed in Table 1. A similar evaluation by Rini et al. [3] calculated that nucleate boiling contributed approximately 35% with a 1 W/cm^2 heat input and 73% with a 10 W/cm^2 heat input. These results are also listed in Table 1. The larger nucleate boiling contribution at 1 W/cm^2 is due to the larger observed site density.

Table 1: Nucleate Boiling Contribution (Fused Silica Heater)

	1 W/cm^2	1.75 W/cm^2	2.9 W/cm^2	1 W/cm^2 [3]	10 W/cm^2 [3]
Bubble frequency, _f_ (bubbles/s)	30	50	70		
Site density, _n_ (sites/cm^2)	25	57	103	61	900
Bubble heat flux (W/cm^2)	0.1	0.4	1.0		
Nucleate boiling contribution	10%	23%	35%	35%	73%

Bubble and Contact Ring Growth Rate

Fused Silica Heater

A bubble life cycle is composed of three stages; bubble growth, bubble

departure, and the waiting time. The outer bubble diameter increases as

the bubble generates vapor and grows larger. As previously observed in

Figure 18, the contact ring grows larger during the bubble growth period

and grows smaller during the bubble departure period. The growth rates

of the bubble and contact ring are examined here to further investigate

the pool boiling heat transfer mechanism. In this section, data using the

second fused silica heater tested in this experiment, the FS-2 heater, is

presented. Results from the second sapphire heater tested, the SP-2

heater, are discussed in the following section. Bubble images were

recorded at multiple locations on the FS-2 heater at three heat flux values;

3 W/cm^2, 4 W/cm^2, and 5 W/cm^2.   Several cavities were observed at

each heat flux; six cavities at 3 W/cm^2 and seven cavities at 4 W/cm^2 and

5 W/cm^2. Measurements of outer bubble and contact ring diameters

were made for 20 bubbles at each heat flux; results for 3, 4, and 5 W/cm^2

are shown in Figures 29-34.
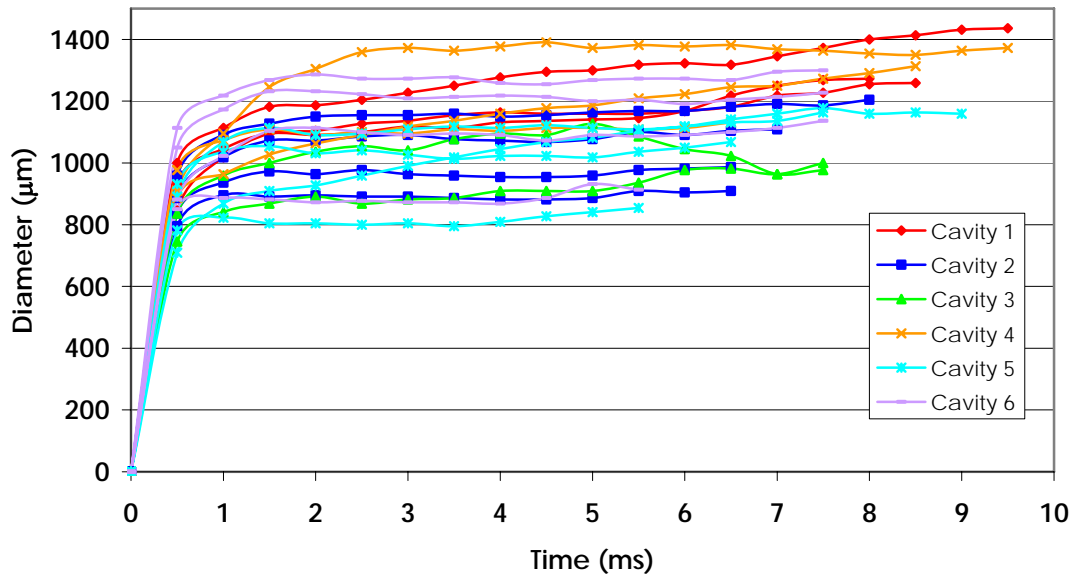
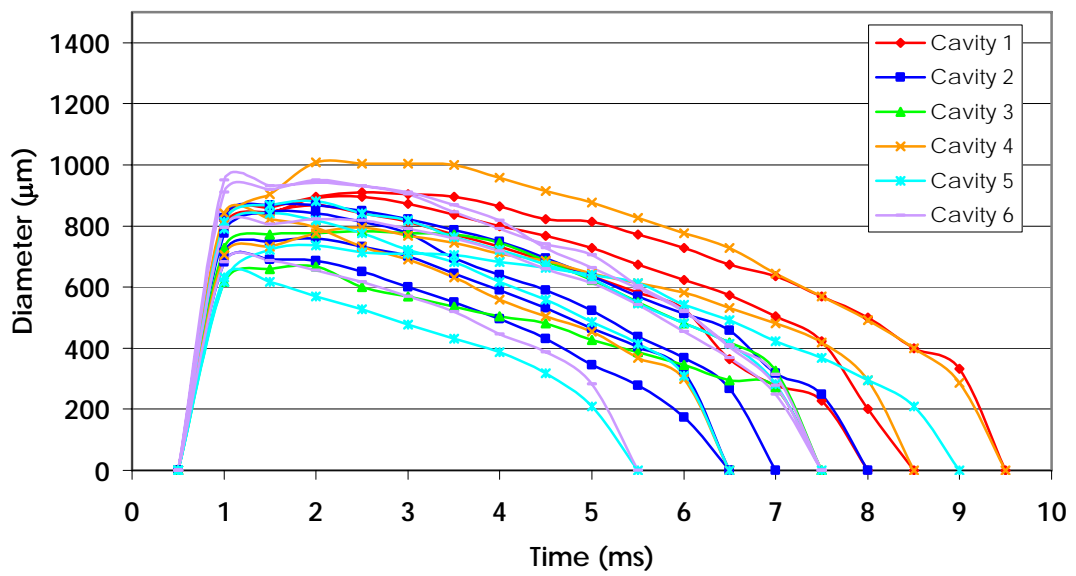**Figure 29: Bubble Diameter at 3 W/cm² (FS-2 heater)**

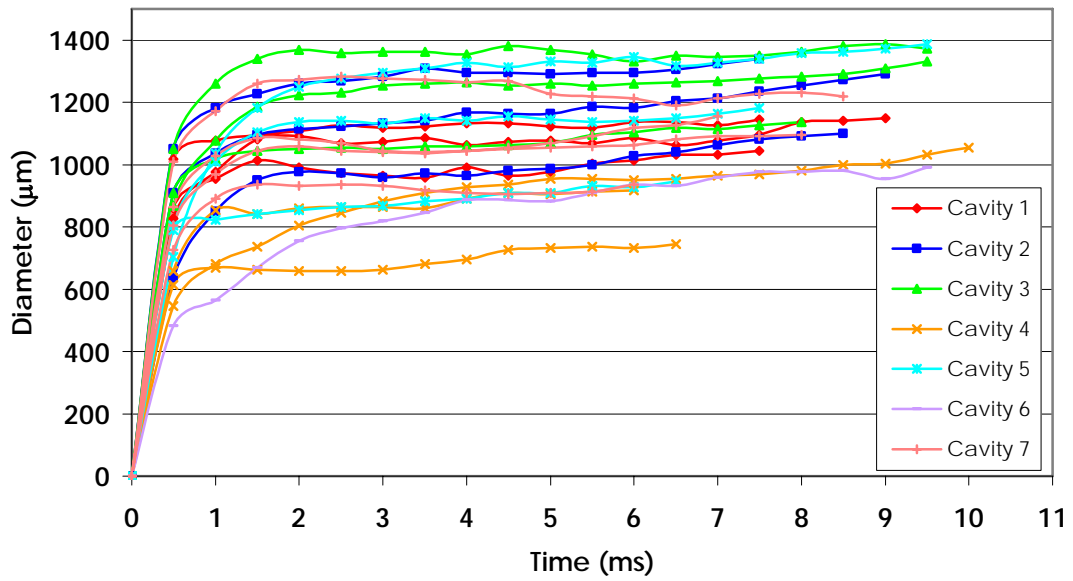**Figure 30: Contact Ring Diameter at 3 W/cm² (FS-2 heater)**

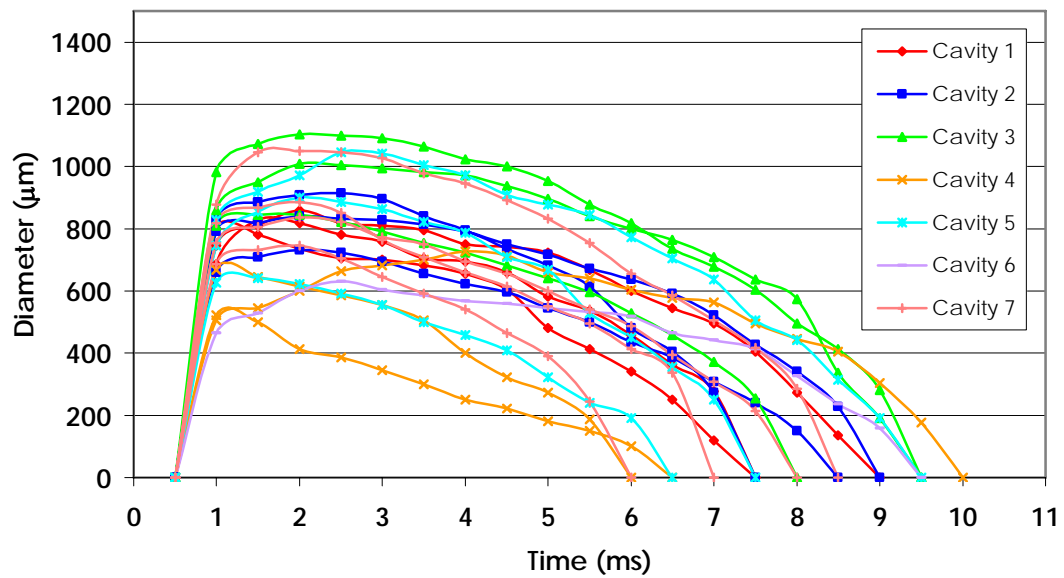**Figure 31: Bubble Diameter at 4 W/cm² (FS-2 heater)**

Figure 32: Contact Ring Diameter at 4 W/cm² (FS-2 heater)
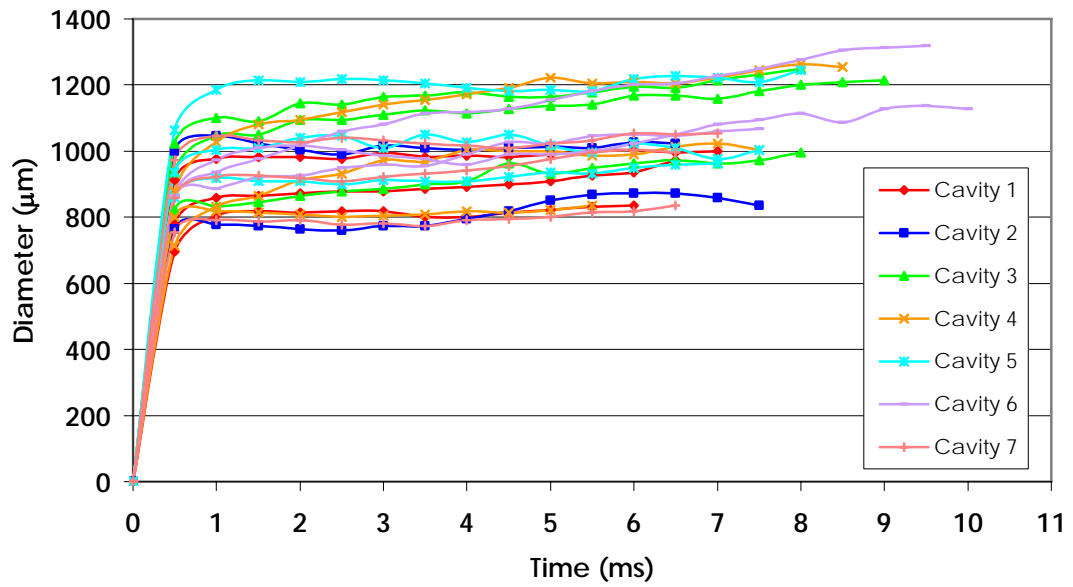
74

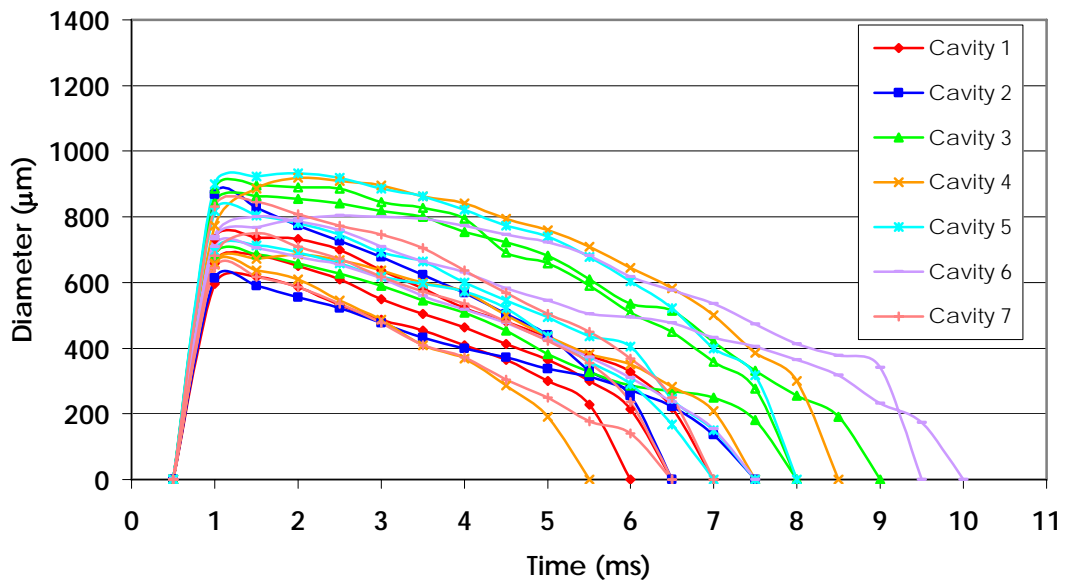**Figure 33: Bubble Diameter at 5 W/cm² (FS-2 heater)**

Figure 34: Contact Ring Diameter at 5 W/cm² (FS-2 heater)

The average bubble departure diameter and lifetime at each heat flux are listed in Table 2.

Table 2: Bubble Departure Diameter and Lifetime (Fused Silica Heater)

	Average Bubble Departure Diameter	Average Bubble Lifetime
3 W/cm^2	1140 μm	7.5 ms
4 W/cm^2	1127 μm	8 ms
5 W/cm^2	1042 μm	7.5 ms

One bubble out of the 20 plotted at each of the three heat fluxes was chosen that best represented the average departure diameter and lifetime noted in Table 2. The bubble and contact ring growth rates for these three bubbles are plotted together in Figure 35. For all three fluxes, the average bubble growth rates, contact ring growth rates, departure sizes, and lifetimes were similar. Therefore it was concluded that the change in heat flux did not affect the bubble departure diameter and lifetime. Similar results have been previously observed for low heat flux values [3].
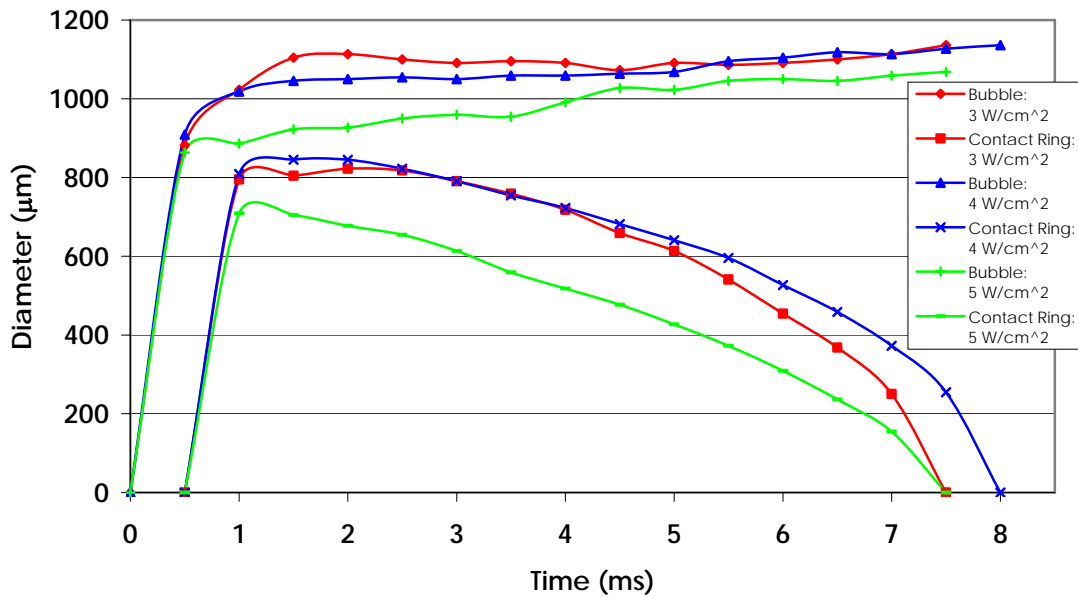
Figure 35: Average Bubble Comparison at Each Heat Flux (FS-2 heater)

Sapphire Heater

Bubble and contact ring growth rate results are plotted for a sapphire heater in Figures 36 and 37. Measurements of the bubble and contact ring diameters for 20 bubbles at 3 W/cm² were recorded from the SP-2 sapphire heater. Bubble data was not recorded at higher heat fluxes from the sapphire heater due to the increased difficulty in distinguishing individual bubble behavior. Seven cavities were viewed at various locations on the bubble heater.
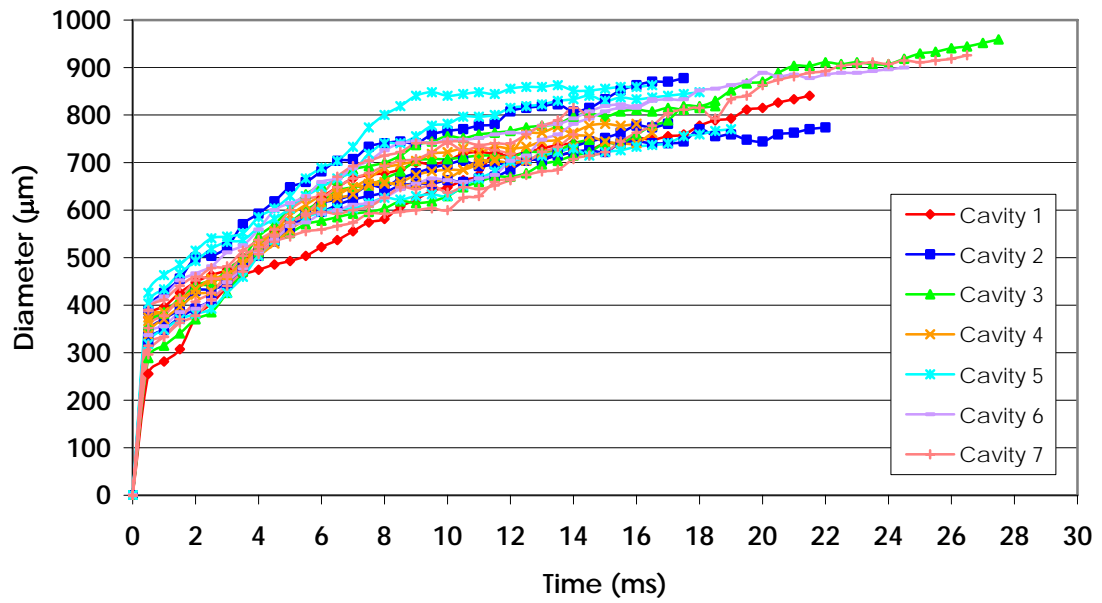
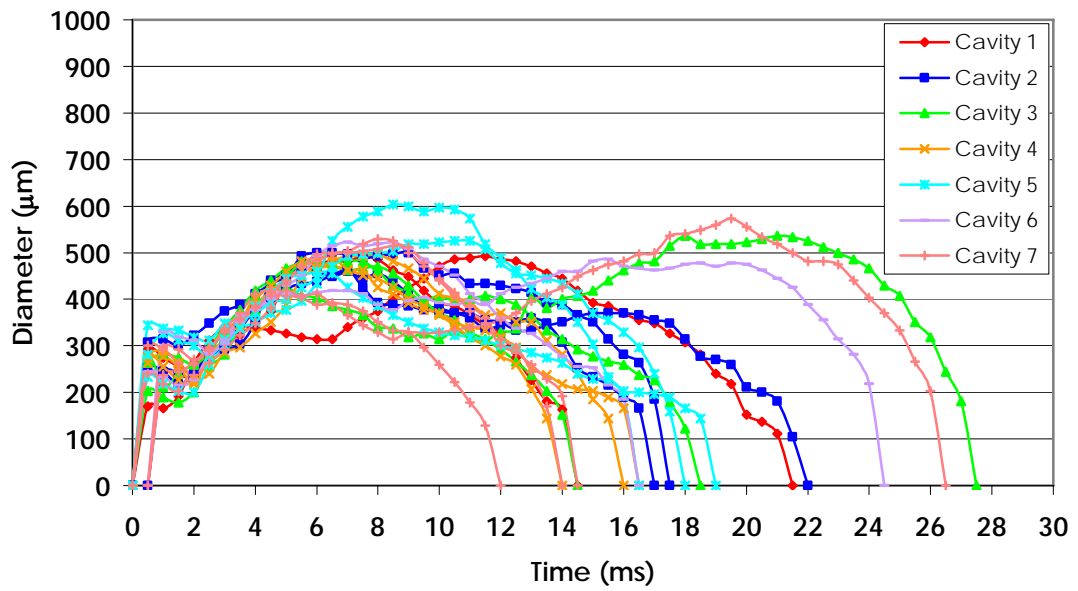**Figure 36: Bubble Diameter at 3 W/cm² (SP-2 heater)**

Figure 37: Contact Ring Diameter at 3 W/cm² (SP-2 heater)

In Table 3 the bubble departure diameter and lifetime results averaged over the 20 bubbles viewed on the sapphire heater are added to the Table 2 results from the fused silica heater for comparison.

Table 3: Bubble Departure Diameter and Lifetime (Sapphire Heater)

	Average Bubble Departure Diameter	Average Bubble Lifetime
Sapphire Heater: 3 W/cm²	809 μm	18 ms
Fused Silica Heater: 3 W/cm²	1140 μm	7.5 ms
Fused Silica Heater: 4 W/cm²	1127 μm	8 ms
Fused Silica Heater: 5 W/cm²	1042 μm	7.5 ms

Based on the average values found in Table 3, the bubbles that grew on this sapphire heater departed at diameters about 300 μm smaller and with lifetimes more than twice the length of the bubbles on the fused silica heater. Again, one bubble out of the 20 plotted at 3 W/cm² for both the fused silica and sapphire heater was chosen that best represented the average departure diameter and lifetime recorded in Table 3. The bubble and contact ring growth rates for these two bubbles are plotted

together in Figure 38 to clearly demonstrate the differences in bubble

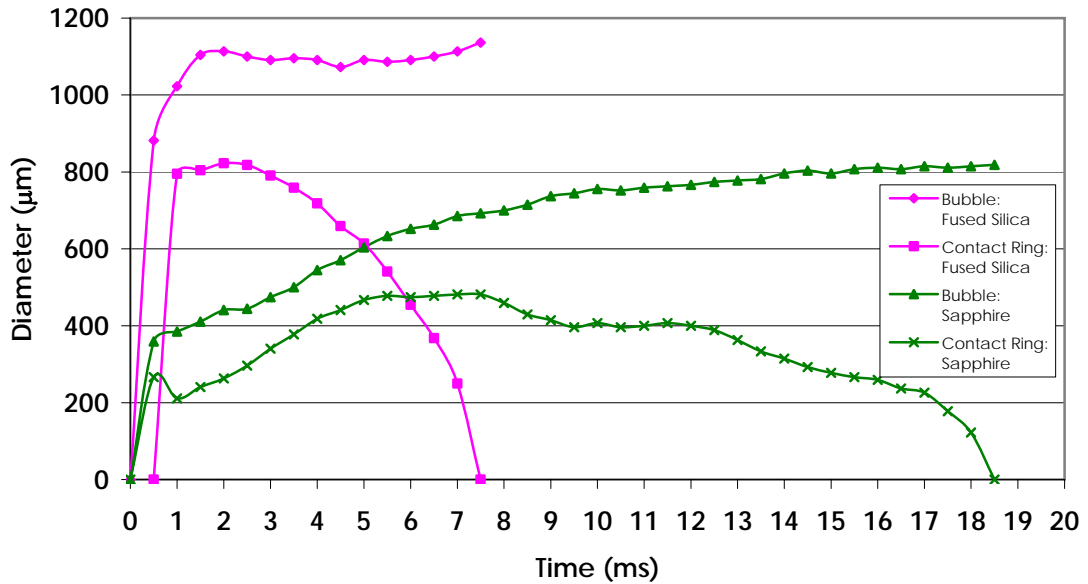behavior on these fused silica and sapphire heaters.

Figure 38: Fused Silica and Sapphire Heater Bubble Comparison

It is apparent from Figure 38 that the bubbles from this fused silica heater

have larger departure diameters and shorter lifetimes than the bubbles

from this sapphire heater. Larger bubbles generally depart from a surface

earlier than smaller bubbles due to the combined effects of buoyancy,

inertial forces, lift, and drag [1]. The buoyancy force, which increases as

the bubble grows larger, eventually overcomes the surface tension forces

at the base of the bubble anchoring the contact ring to the surface. The

inertia forces produced by the movement of the liquid-vapor interface during bubble growth also contribute to a bubble's departure, especially during rapid bubble growth as observed in the first 0.5 ms of the fused silica bubble lifetime in Figure 38.

Visual observations of the fused silica and sapphire heater surfaces during 3 W/cm² pool boiling showed that the sapphire heater generated larger bubble frequencies and larger bubble site densities than the fused silica heater. This was likely due to the higher thermal diffusivity and the associated increased lateral heat conduction of the sapphire heater. The sapphire heater was better able to replenish the depleted energy supply at the heater surface after a bubble departure, allowing the surface and liquid layer to reheat more rapidly so a new bubble could form.   Also the sapphire heater could more efficiently distribute its energy supply to all potential cavities.

In Equation 10 the bubble departure frequency, f, is related to the bubble growth time, t_g, and the waiting time, t_w [1].

$$\frac{1}{f} = t_g + t_w \qquad (10)$$

For these fused silica and sapphire heaters, the growth time, t_g, was acquired from the data in Figure 38 and the frequency, f, was obtained by averaging the frequency values observed from four different cavities during one second of bubble nucleation on each heater. These values and the calculated bubble waiting times, t_w, for each heater are listed in Table 4.

Table 4: Bubble Waiting Time at 3 W/cm²

	Bubble Frequency	Bubble Growth Time	Bubble Waiting Time
Fused Silica Heater	21 bubbles/s	7.5 ms	40 ms
Sapphire Heater	30.5 bubbles/s	18 ms	15 ms

These calculations show that the waiting time for bubbles on this fused silica heater was typically more than double the waiting time for bubbles on this sapphire heater. The data suggests that the larger thermal diffusivity of the sapphire heater did improve the energy supply available for bubble nucleation at the heater surface, shortening the waiting time after bubble departure before the next bubble could begin to grow.

Based on the shape of the plots in Figure 38, it is evident that the bubble growth behavior significantly differed for these fused silica and sapphire heaters. The fused silica heater bubble showed a very rapid growth in the first 0.5 ms of its lifetime. The contact ring reached its maximum diameter almost immediately, and bubble departure began as soon as the contact ring began to shrink. This signifies that the microlayer completely evaporated in the first 2 ms, and that the bubble was departing during the remaining 5.5 ms of the bubble lifetime. The sapphire heater bubble, on the other hand, experienced a more gradual growth rate and slower microlayer evaporation. The contact ring exhibited some oscillating behavior, as previously seen in Figure 22, before the bubble began to depart at 12 ms. Bubbles from both heaters consistently displayed similar lengths of time to depart from the heater surface; approximately 5.5 ms and 6.5 ms for the fused silica and sapphire bubbles, respectively, in Figure 38.

This rapid bubble growth detected from the bubbles on the fused silica heater suggested possible inertia-controlled growth instead of heat-transfer-controlled growth. The bubble transition radius from inertia-controlled to heat-transfer-controlled growth was estimated with the

relationship for bubble growth in a superheated liquid pool, seen in Equation 11 [1].

$$R_{trans} = \frac{12\alpha_l (T_w - T_{sat})^2 \rho_l^2 c_p^2 \sqrt{\rho_l T_{sat}}}{\pi \rho_v^2 h_{fg}^2 \sqrt{2(T_w - T_{sat})h_{fg}\rho_v}} \qquad (11)$$

Using the property values for FC-72 listed in Table 5 and a superheat, T_w-T_{sat}, of 13 K determined from the experiment, the transition radius was calculated to be approximately 6 µm. This small diameter value confirmed that essentially all of the bubble growth in this experiment is heat-transfer-controlled and that inertia-controlled growth is insignificant. Therefore, the energy available to a bubble is the limiting factor in bubble growth.

Table 5: FC-72 properties

Latent heat of vaporization, h_{fg}	88 kJ/kg
Vapor density, ρ_v	14 kg/m³
Liquid density, ρ_l	1680 kg/m³
Thermal diffusivity, α_l	3.08 x 10⁻⁶ m²/s
Specific heat, c_p	1100 J/kg-K
Saturation temperature, T_{sat}	329 K

The source of this additional energy supplied to the bubbles on this fused

silica heater is still in question. Limited bubble growth data from the FS-1

fused silica heater indicated that not all fused silica heaters would

demonstrate such extreme microlayer evaporation and bubble growth.

For comparison, note that the first fused silica heater had a bubble

departure frequency of 70 bubbles/s at 2.9 W/cm^2. The second fused

silica heater had a frequency of 21 bubbles/s at 3 W/cm^2. The smaller

bubble frequency of the second fused silica heater corresponds to longer

waiting times, and the physical characteristics of a cavity are known to

affect the bubble waiting time [1]. Therefore it is likely that the surface

condition of this particular fused silica heater contributed to its unusual

bubble behavior.

Local Heat Transfer Curves

Surface temperature information from the natural convection and

nucleate boiling portions of the pool boiling curve were recorded and

plotted at varying heat fluxes. Between each successive measurement

the desired input heat flux was obtained by adjusting the voltage applied

to the heater. The temperature value of every data point on the graphs is

an average of the 50000 temperature measurements recorded over one second by the DAQ. These temperatures were measured by the TFTCs and are considered local temperature values.

Figure 39 shows a sample heat flux curve acquired from an inner TFTC on the second fused silica heater, FS-2, tested in this experiment.
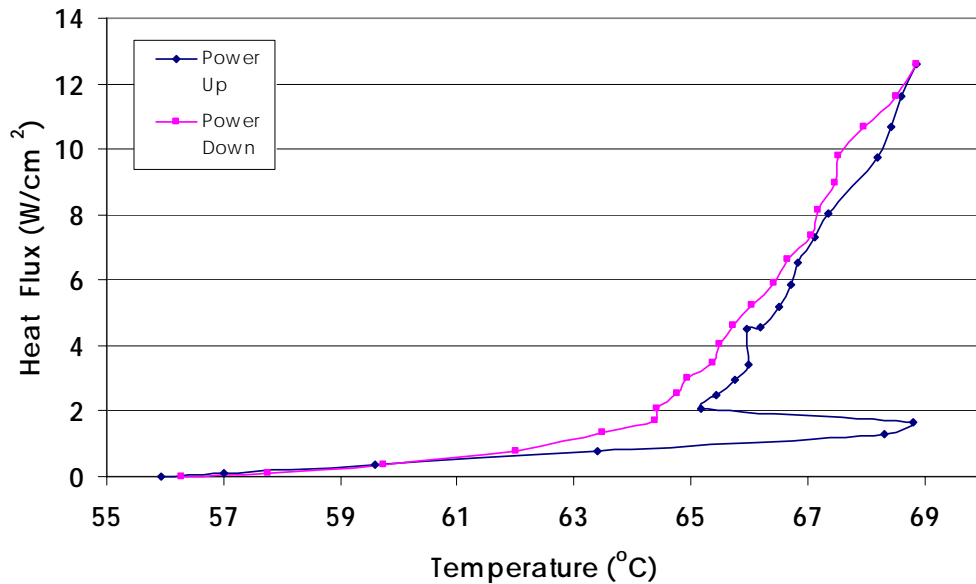

Figure 39: Fused Silica Heat Flux Curve from Zero Heat Flux (FS-2 heater)

The input power started from zero and was gradually increased to a final heat flux value greater than 12 W/cm^2, seen in the "Power Up" curve. Initially at about 56°C, the saturation temperature of FC-72, the surface

temperature increased with the increase in heat flux until the onset of nucleate boiling was reached at almost 69°C, a surface superheat of 13°C. This temperature overshoot to a higher superheat was required to initiate boiling due to the tendency of highly wetting fluids like FC-72 to fill the cavities with liquid instead of the vapor needed to activate the cavity. Once bubble growth began, the surface temperature dropped approximately 4°C from about 69°C to 65°C. This sudden drop occurred because the heat transfer coefficient increased considerably during the transition from natural convection to nucleate boiling [17, 18].   Smaller superheat values were then sufficient to sustain bubble nucleation because bubbles departing from the surface left behind larger quantities of vapor in the cavities than were initially present on the wetted surface.

From 2 W/cm^2 to 12 W/cm^2 in Figure 39, the surface temperature continued to increase with an increase in heat flux. More bubbles appeared as additional cavities were activated, possibly due to vapor sharing between active and dormant cavities [18, 19]. Vapor sharing occurred when a bubble grew over a nearby, inactive site, leaving sufficient vapor behind in that cavity to initiate growth. Only a limited range of the cavity sizes were eligible to become active nucleation sites [20]. Some cavities were too small to be activated before higher

superheat values were attained, and some cavities were too large to produce moderate size bubbles growing within the superheated liquid layer [1].

The slope of the curve, and consequently the heat transfer coefficient, was much higher in this nucleate boiling region than in the natural convection region. At 12 W/cm^2 the heat flux was then decreased back to zero on the "Power Down" curve, which followed the typical nucleate boiling curve. Heat flux curves with temperature overshoots resembling the ones shown in Figure 39 have been observed in other experiments with highly wetting liquids where the average instead of the local surface temperature was monitored [3, 17, 18, 19, 21]. Cavities initially have less trapped vapor with a wetting fluid such as FC-72, requiring a larger superheat to activate the cavities and thereby producing the observed temperature overshoot.

Figure 40 is an example of a heat flux curve from the same FS-2 fused silica heater, where the power input on the "Power Up" curve was started at 1 W/cm^2 instead of zero. This curve showed no indication of the type of temperature overshoot described above, and in fact was comparable to the "Power Down" curve observed in Figure 39. Apparently the superheat

that was maintained at 1 W/cm^2, slightly larger than 7°C, prevented the cavities from becoming deactivated. This behavior was consistently observed in the additional 14 curves performed in this experiment that were started from 1 W/cm^2, including the one shown in Figure 42. The "Power Down" curve followed the typical nucleate boiling curve, as expected.
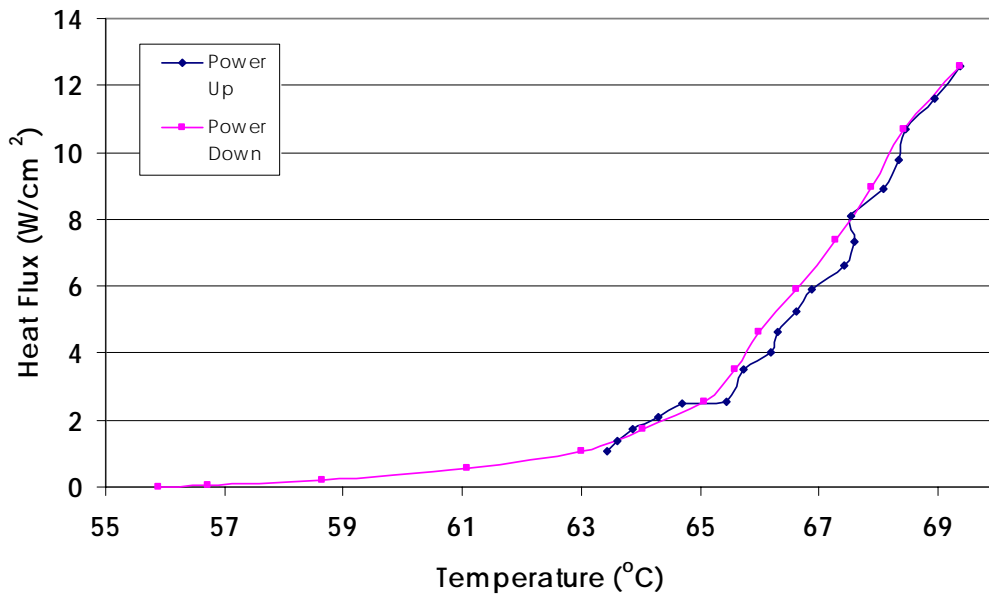

Figure 40: Fused Silica Heat Flux Curve from 1 W/cm^2 (FS-2 heater)

The set of heat flux curves located in Figure 41 were recorded from the second sapphire heater, SP-2, tested in this experiment, unlike the previous curves from the fused silica FS-2 heater.   Measurements from two different

TFTCs, {a} and {b}, were plotted; the results from TFTC {a} can be viewed in

this graph. There are two sets of "Power Up" and "Power Down" curves;

both were started from a zero power level comparable to Figure 39.
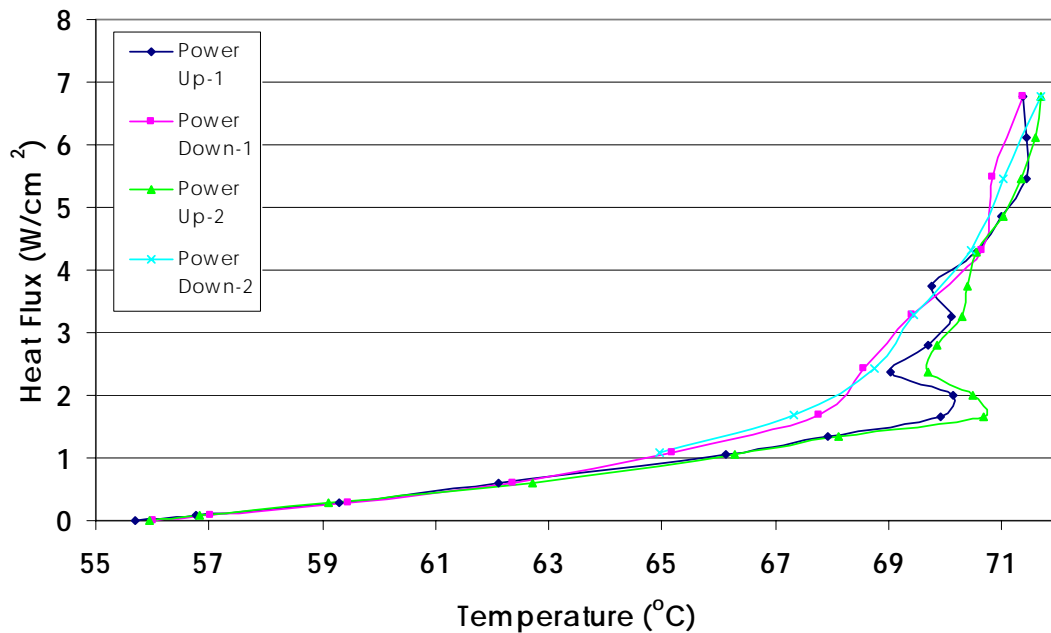
Figure 41: Sapphire Heat Flux Curves from Zero Heat Flux

TFTC {a} (SP-2 heater)

A temperature overshoot of less than 3°C was observed in these two sets

of curves. Additional heat flux curves from TFTC {a} demonstrated both

higher and lower overshoot magnitudes than the ones seen here. This

variation in the data is believed to be due to the highly localized

temperature measurements that create these curves, as opposed to the customary method of using average surface temperatures to plot heat flux curves [3, 17, 18, 19, 21]. Surface and boiling conditions directly on and around the TFTC junction could influence the details of the temperature behavior.

The heat flux curves presented in Figure 42 were recorded from the other TFTC on the sapphire heater, TFTC {b}. The first two sets of curves began from a zero power input while the third set of curves began from 1 W/cm², similar to Figure 40. The third set of curves followed the typical nucleate boiling curve without a temperature overshoot as the power was increased and decreased.

A large temperature overshoot, approximately 8°C, was observed in the first two sets of curves at 1-2 W/cm², but the temperature did not drop back to the typical curve as seen in the previous graphs. The temperature fell only about 2°C at the onset of nucleate boiling, and then increased with increasing heat flux following a slope similar to that of the typical curve. At about 8 W/cm² the temperature dropped again to a slightly lower temperature than that of the typical curve, and then recovered to meet the typical curve at about 10 W/cm².
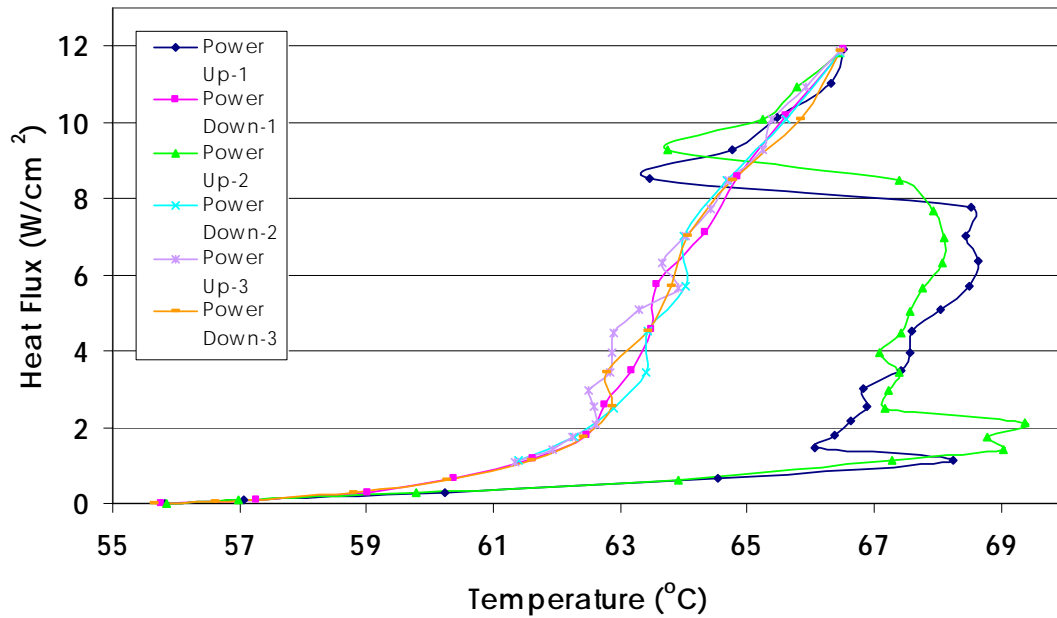
Figure 42: Sapphire Heat Flux Curves from Zero and from 1 W/cm² TFTC {b} (SP-2 heater)

This unusual temperature drop, typically arising between 6 and 9 W/cm², occurred repeatedly throughout the course of this experiment on the SP-2 heater at TFTC {b}. It appeared to be a characteristic of this specific TFTC location and most likely occurred due to the delayed triggering of cavities in the TFTC region. This delay was possibly caused by a lack of vapor sharing at the lower heat fluxes due to the size, structure, or distribution of the cavities in the area immediately surrounding the TFTC {b} junction. This, along with variations in the surface temperature behavior under

similar heat flux conditions, suggested that the local surface condition had a significant effect on the local heat flux curves.

A final set of curves from TFTC {b} on the SP-2 sapphire heater, shown in Figure 43, investigated the effect of a power time delay on the nucleate boiling curves.
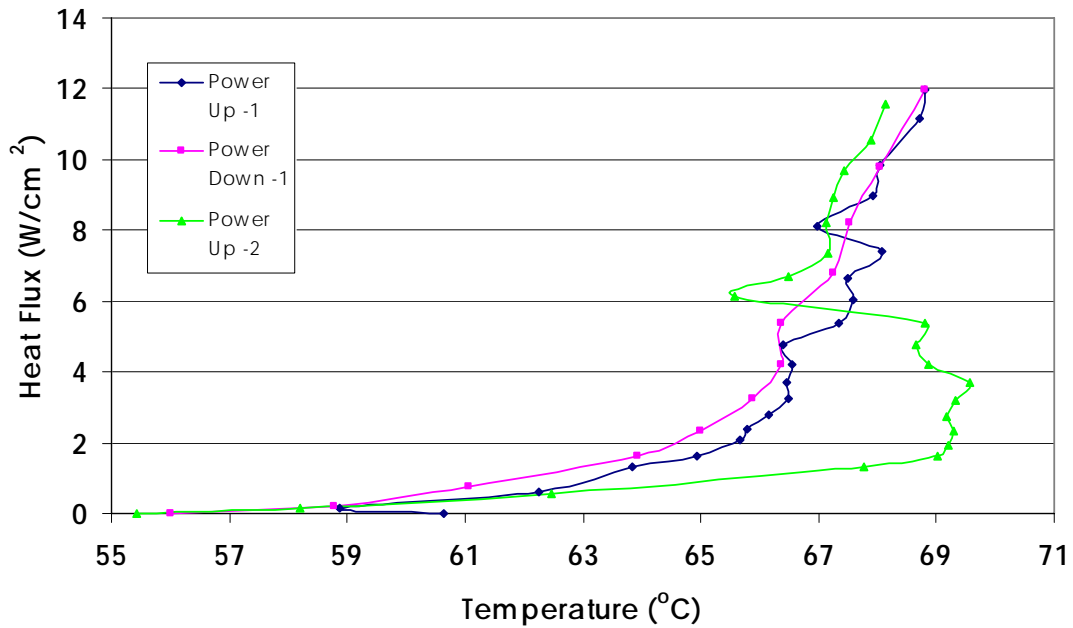
Figure 43: Sapphire Heat Flux Curves from Zero Heat Flux with Power Time Delay and No Power Time Delay TFTC {b} (SP-2 heater)

After boiling occurred on the heater the power was returned to zero, and the length of time before power was input to the heater again was known as the power time delay. All of the previous curves with temperature overshoots from the FS-2 and SP-2 heaters began from a zero power input, and they had a power time delay of at least 10-15 minutes before the heat flux was increased. Other studies have suggested that certain waiting periods [17] or surface aging procedures [19] prevented these temperature overshoots from occurring.

The first "Power Up" curve in Figure 43 was increased from zero with no power time delay, and showed no evidence of a temperature overshoot. The second "Power Up" curve was increased from zero after a 30 minute time delay, and the temperature overshoot was obviously present. Additional tests showed that even power time delays as short as two minutes could trigger the temperature overshoot. It was determined that only a negligible time delay before the heat flux was increased from zero could ensure that the temperature overshoot would not occur. Any length of time could prove long enough, with a highly wetting fluid like FC-72, for liquid to refill or for vapor to recondense in the cavities.

CONCLUSIONS

A transparent heater with four thin film thermocouples has been developed to measure the surface temperature fluctuations that occur during pool boiling bubble nucleation. Correlations between bubble images and temperature measurements demonstrated that the surface temperature dropped whenever the bubble contact ring crossed over the TFTC junction. This set of temperature drops was caused by microlayer evaporation during bubble growth and the liquid rewetting the heater surface during bubble departure. These observed temperature drops were relatively small and were of similar magnitude and time duration, disputing the theory that microlayer evaporation is the dominant pool boiling heat removal mechanism.

Temperature measurements recorded from heaters with fused silica and sapphire insulation layers revealed that the sapphire heaters did not exhibit the same observable temperature drops during bubble nucleation that were detected from the fused silica heaters. This difference was concluded to result from the 18 times larger thermal diffusivity, and greater lateral heat conduction, of the sapphire layers. Devices

composed of high thermal diffusivity materials could be recommended to ensure a more uniform surface temperature during nucleate boiling at a specific heat flux.

Details about nucleate boiling heat contribution and bubble and contact ring growth rates were evaluated by examining bubble behavior at varying heat fluxes. Calculations revealed that less than half of the heat removed from the surface at low heat fluxes was due to bubble vapor generation. Observations also showed that the average bubble departure diameter and lifetime did not significantly change with an increase in heat flux. Bubble size, lifetime, departure frequency, and site density, as well as the rate of microlayer evaporation, varied on different heaters due to substrate thermal properties and surface conditions.

As the input heat flux was increased along the nucleate boiling curve, the surface temperature dropped at the onset of nucleate boiling and occasionally again at higher heat fluxes. Bubble formation significantly increased the heat transfer coefficient at the surface, causing this temperature drop, and the resulting smaller superheats were sufficient to sustain bubble growth. Lowering the input heat flux to less than 1 W/cm^2 or returning the heat flux to zero for any length of time caused the highly

wetting liquid to replace the available vapor in the cavities, rendering the

cavities inactive and producing the observed temperature overshoots in

the subsequent curves.

RECOMMENDED FUTURE WORK

Some of the bubble behavior and surface temperature results reported in this research varied under similar heat input conditions, often dependent on which heater was being tested at the time. Bubbles from the fused silica and sapphire heaters displayed different departure diameters, lifetimes, and growth rates. However, the two fused silica heaters in this experiment also produced bubbles with differing growth rates and departure frequencies. Some of the differences between the fused silica and sapphire heater bubbles were likely due to the difference in thermal properties of the two materials, and some of the differences between all of the heaters were likely due to surface conditions, particularly surface roughness and the sizes and profiles of the cavities. Further experimentation with additional fused silica and sapphire heaters could help confirm the source of the variations observed in bubble growth behavior from different heaters.

The contribution of bubble nucleation to the total heat transfer removed from a surface during nucleate boiling was calculated in this experiment for one of the heaters with a fused silica insulation layer. Similar

calculations for the nucleate boiling contribution from a sapphire heater would be valuable to further investigate the impact of heater substrate thermal diffusivity on the pool boiling heat transfer mechanism.

Wide variations in the temperature behavior of the heat transfer curves were detected in this study. The temperature overshoots that are typically observed in pool boiling curves with highly wetting fluids like FC-72 did occur, although they differed in magnitude, surface superheat, and heat flux when recorded on separate heaters, on the same heater at different TFTC junction locations, and sometimes at the same TFTC junction on different days. The data points plotted in these heat transfer curves were averaged over one second of time, and each data point was recorded at a quasi-steady state condition between the adjustments in heat flux input levels. If temperature data could be recorded during the transient period when the input heat flux is being adjusted, and bubble images could also be observed during this time, it would be possible to monitor the actual temperature drops as they occur and the bubble behavior that affects them. A clarification of the cause of these differences in the temperature drops due to a change in input heat flux could be achieved.

APPENDIX A: EXPERIMENT DESIGN DRAWINGS
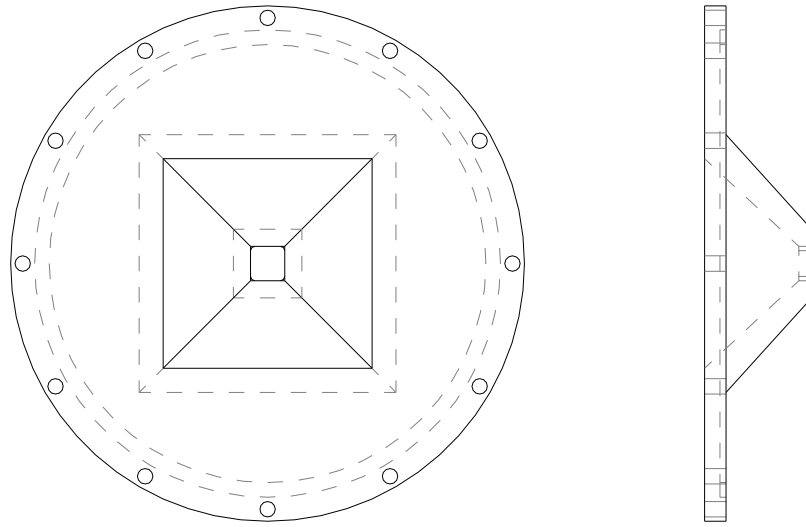
Figure 44: Pyramid Top and Side View

Tap 8x32
0.75" deep

Acrylic
Top and Bottom
(inches)

30°

2.8600

R2.5000

R3.0000
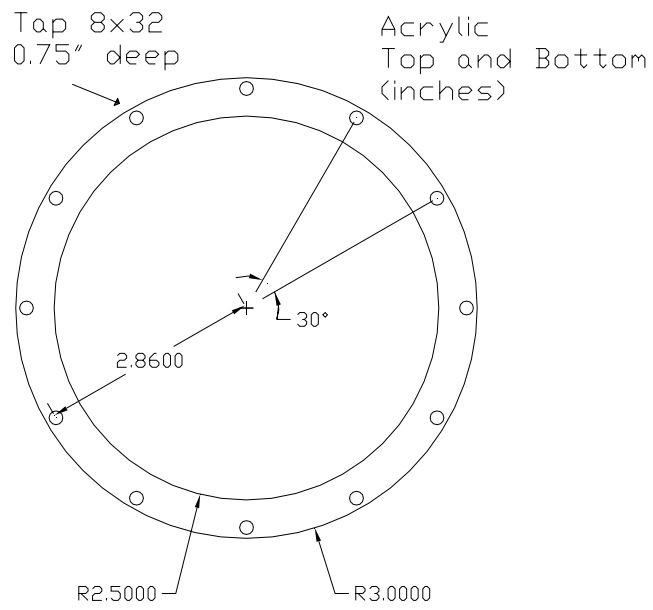
Figure 45: Chamber Top and Bottom View
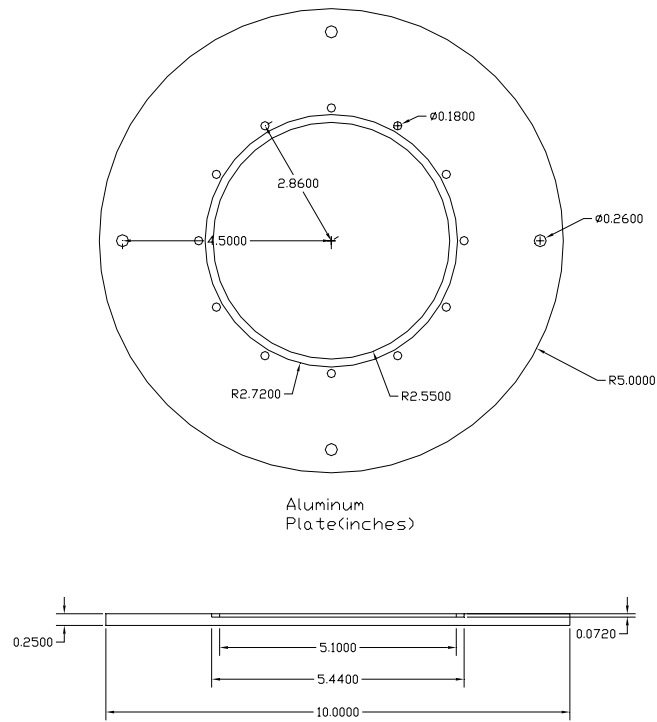
Figure 46: Aluminum Condenser Plate
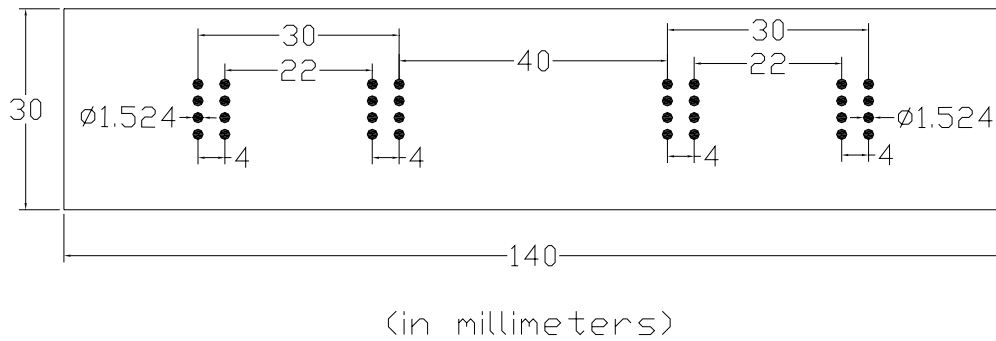
Figure 47: TFTC Epoxy Holder

APPENDIX B: EXPERIMENT PHOTOS
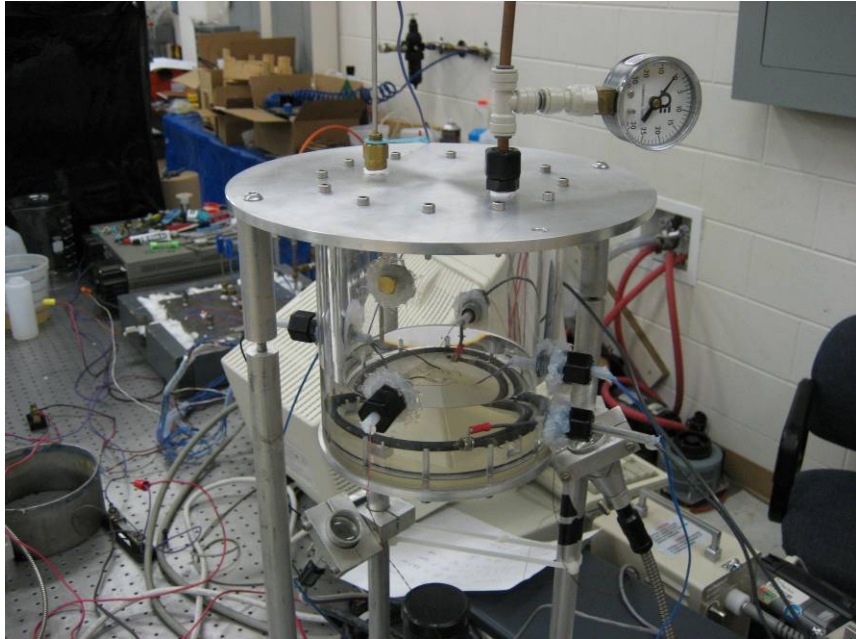
Figure 48: Photograph of Chamber

Figure 49: Side View Photograph of Chamber
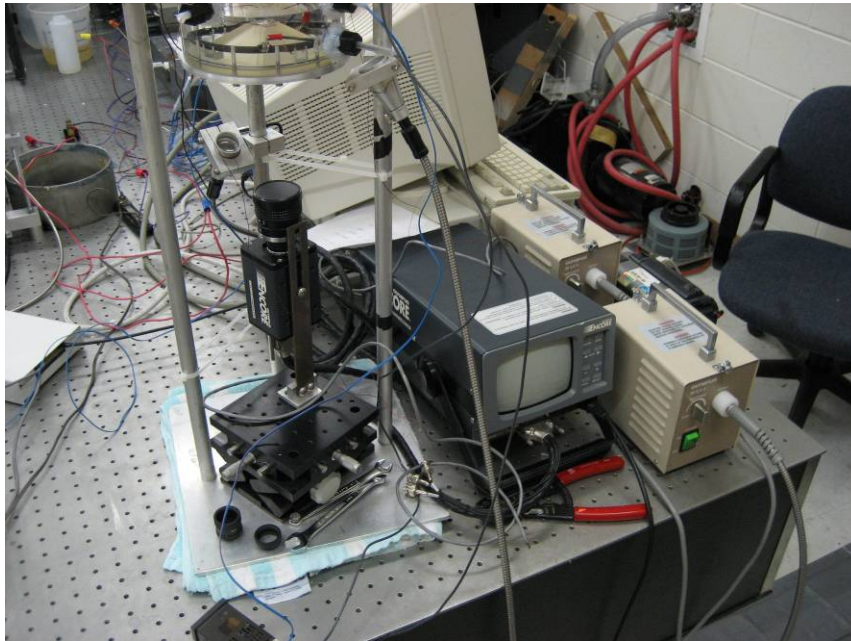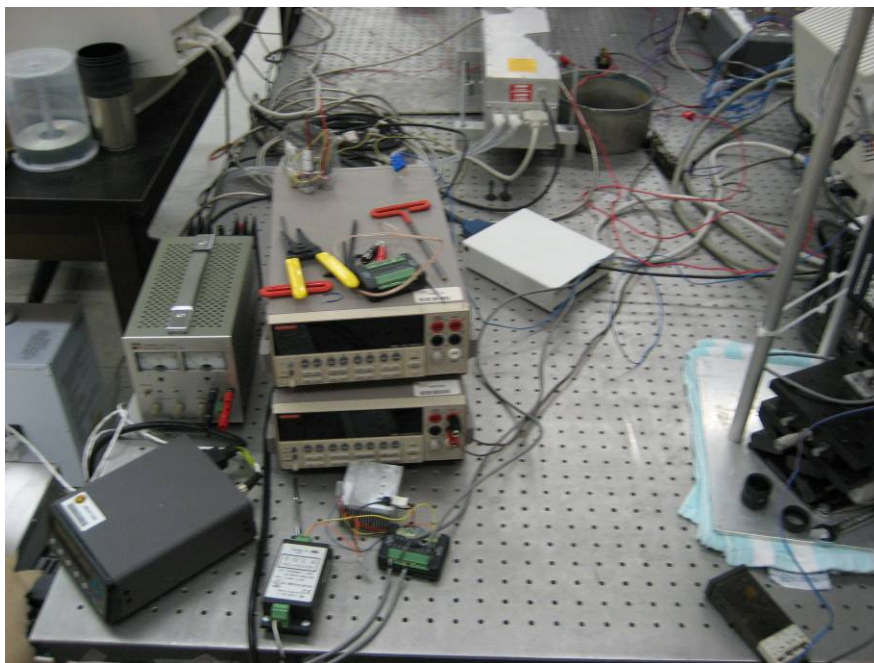
Figure 50: Photograph of Camera and Lighting System

Figure 51: Photograph of Power System and TC Amplifier
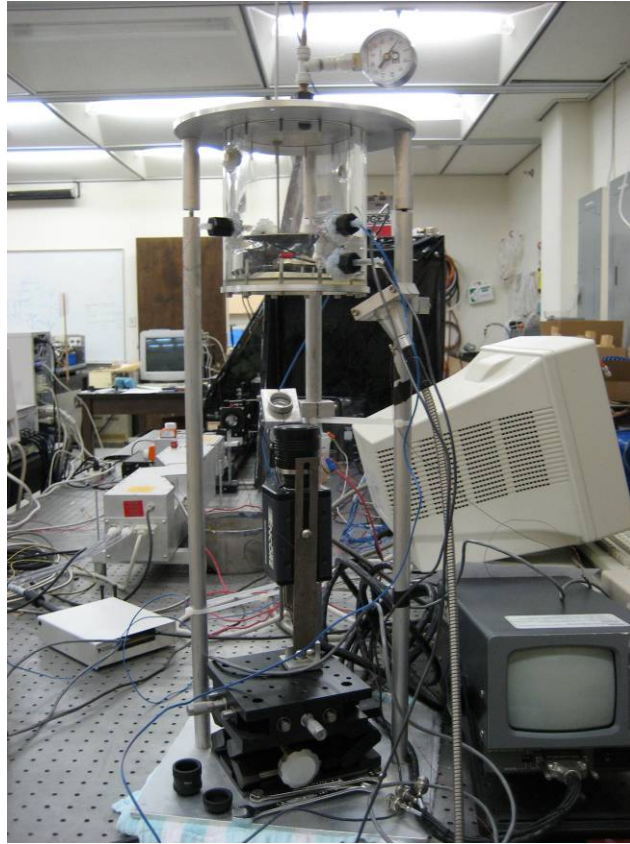
Figure 52: Photograph of Chamber and Camera System
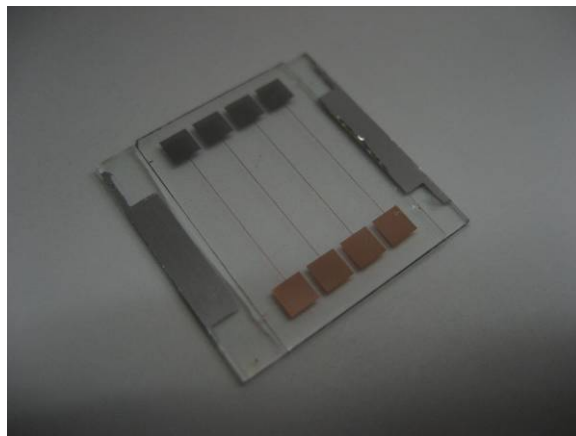
Figure 53: Photograph of Heater

APPENDIX C: SIMULATION RESULTS
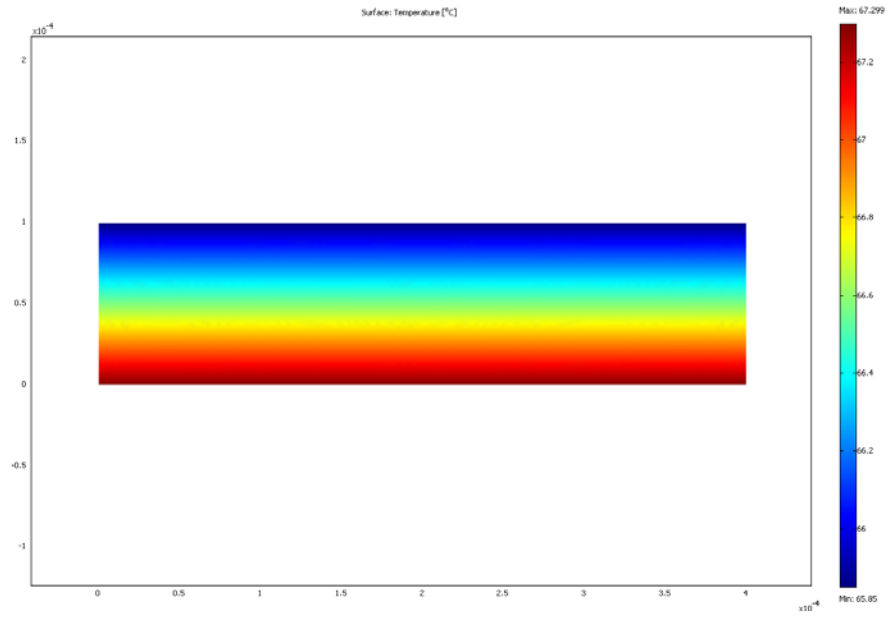
Figure 54: Fused Silica Heater Simulation Results: Steady-State
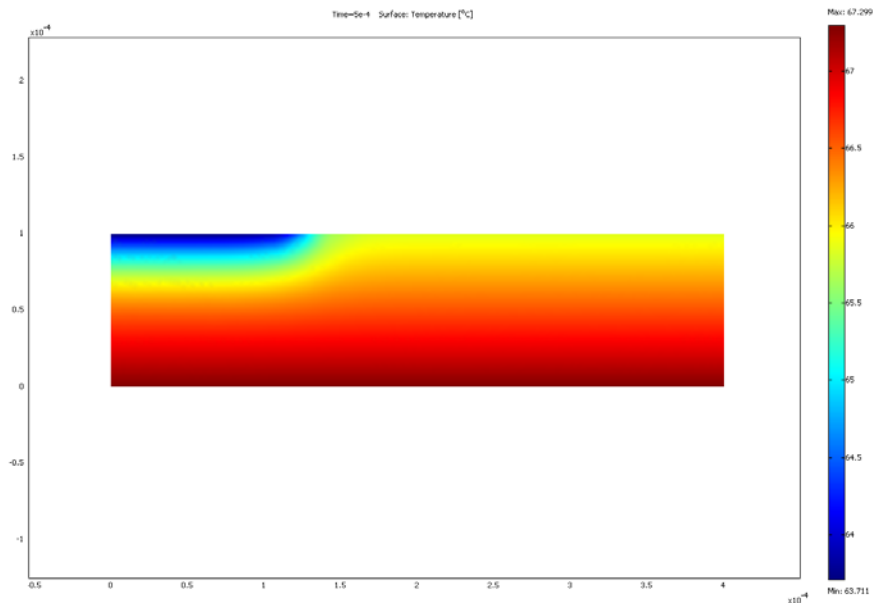
Figure 55: Fused Silica Heater Simulation Results: First Time Step
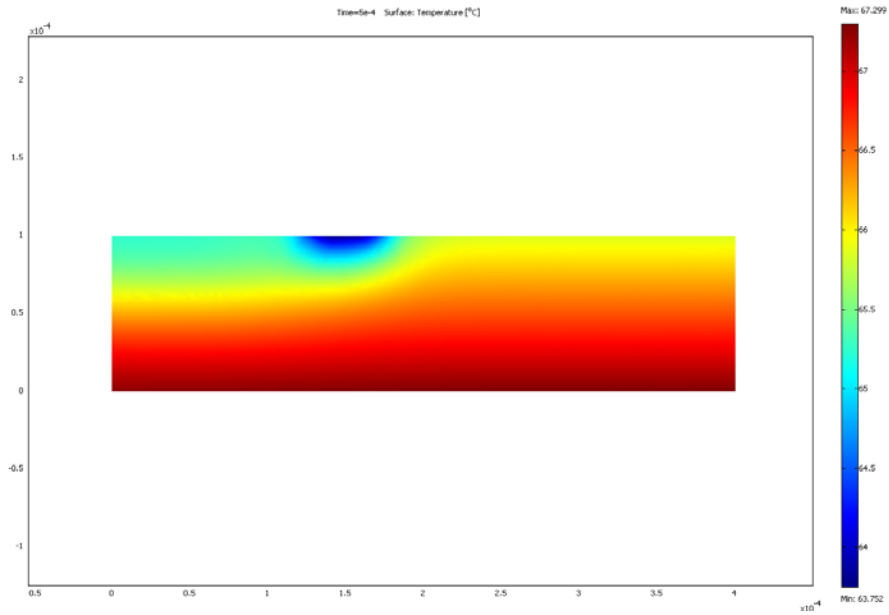
Figure 56: Fused Silica Heater Simulation Results: Second Time Step
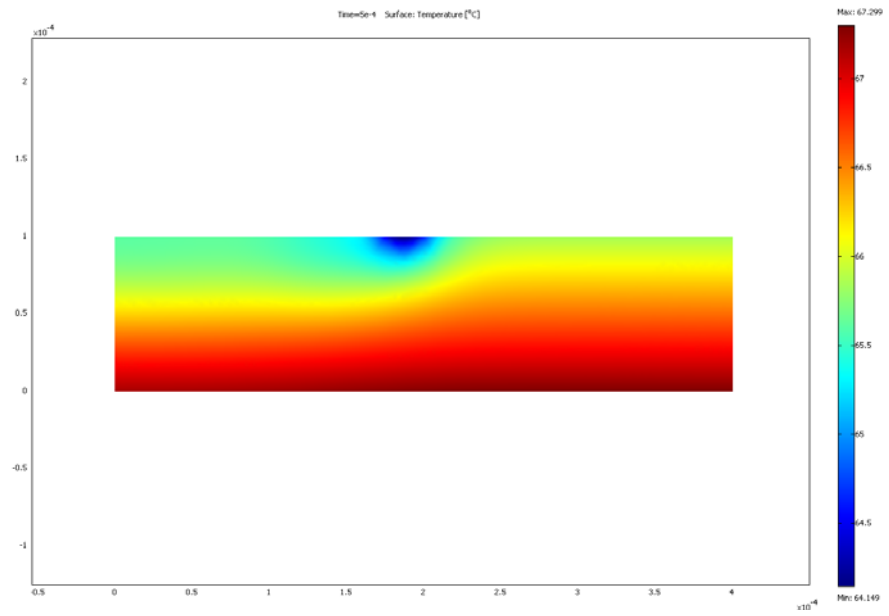
Figure 57: Fused Silica Heater Simulation Results: Third Time Step
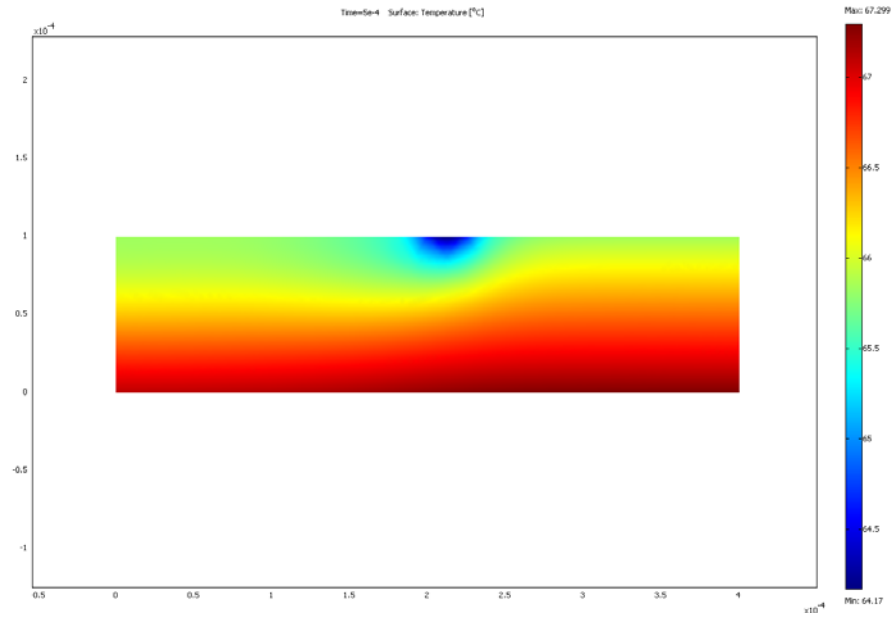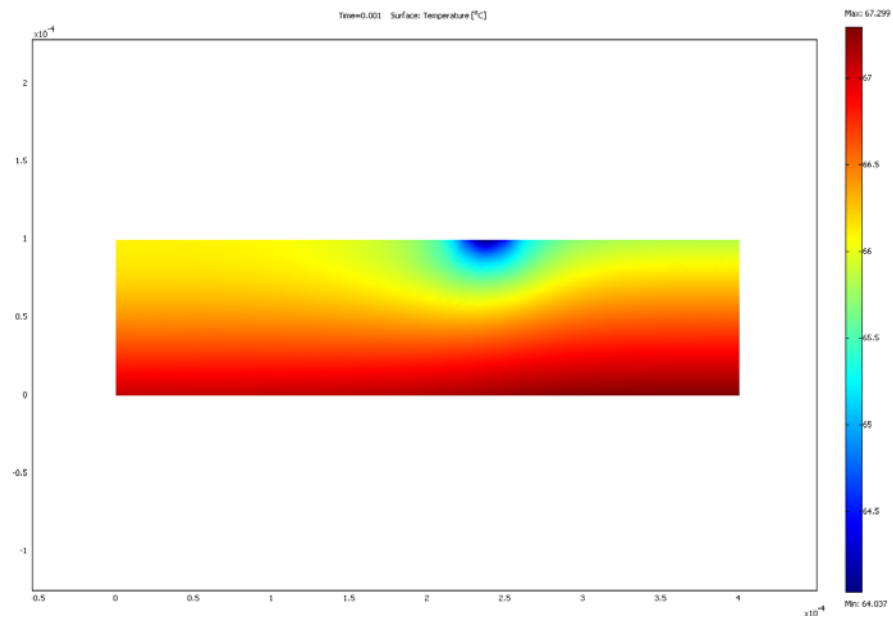
Figure 58: Fused Silica Heater Simulation Results: Fourth Time Step

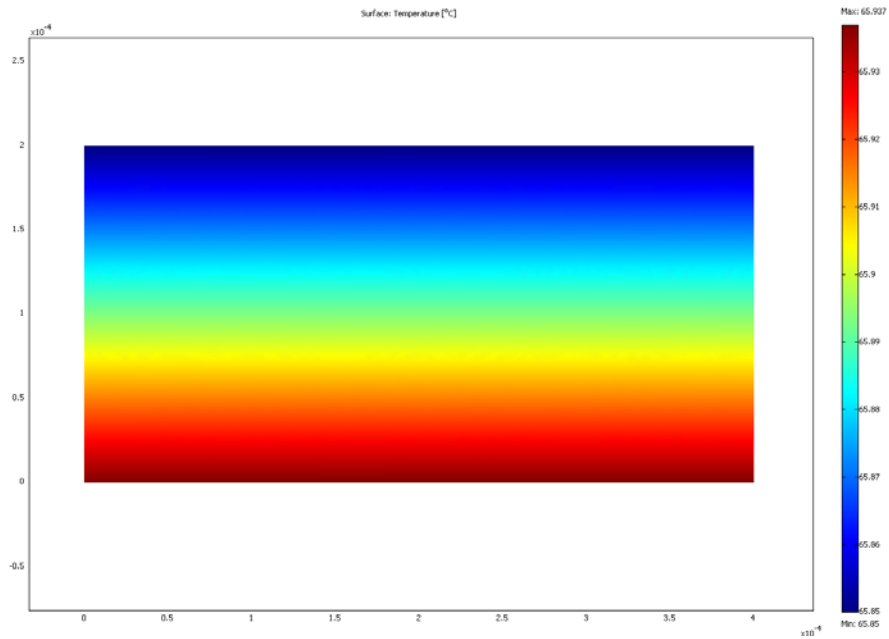**Figure 59: Fused Silica Heater Simulation Results: Final Time Step**

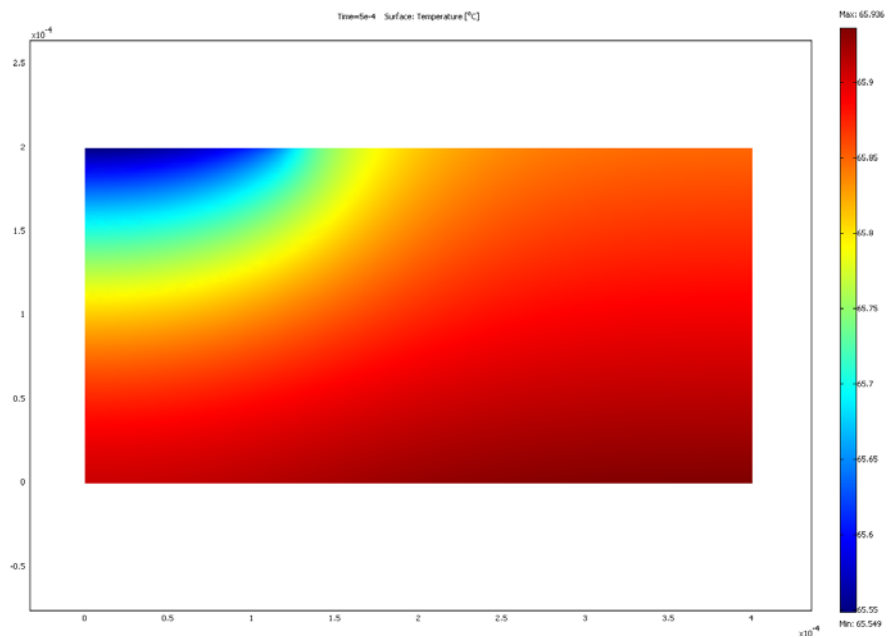**Figure 60: Sapphire Heater Simulation Results: Steady-State**

Figure 61: Sapphire Heater Simulation Results: First Time Step
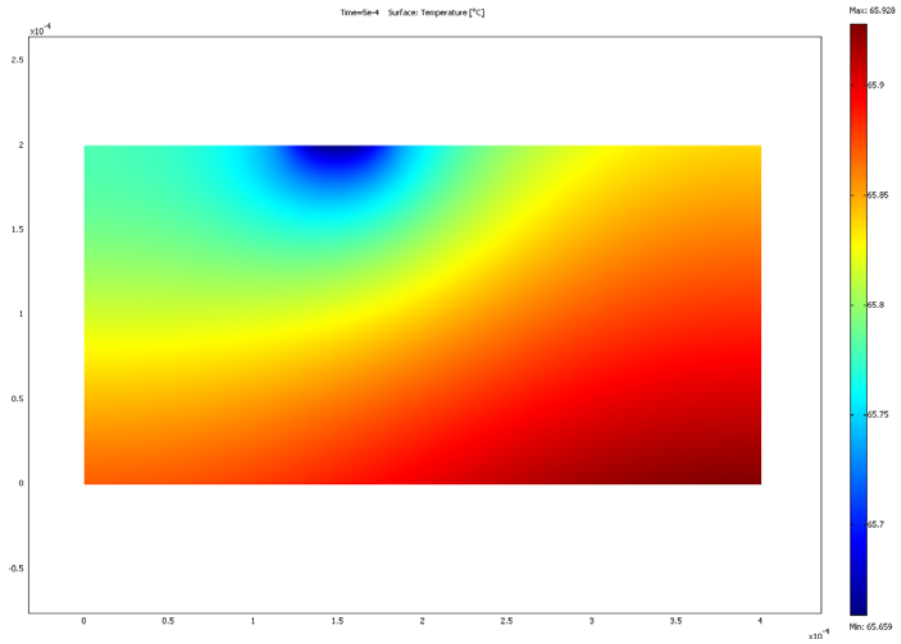
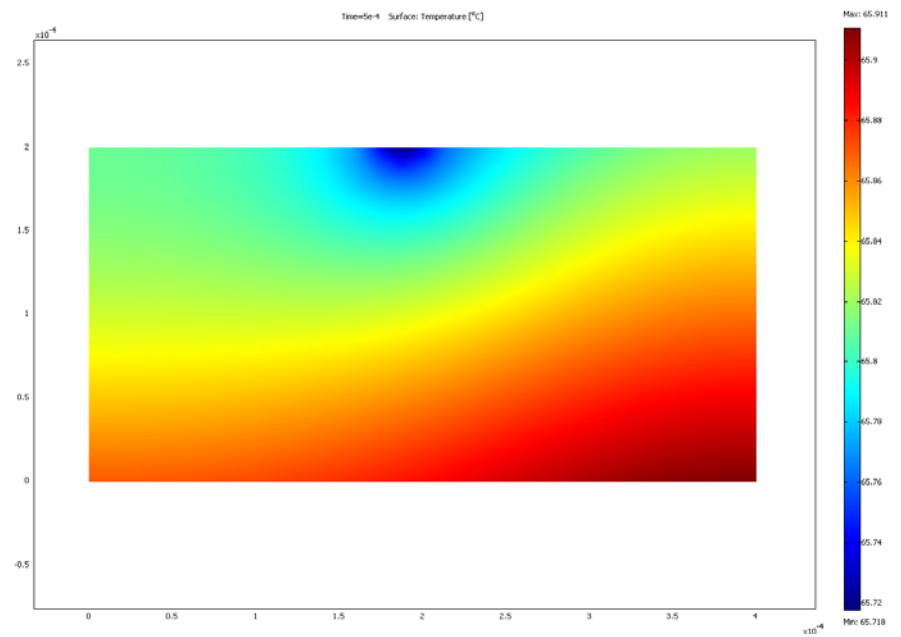**Figure 62: Sapphire Heater Simulation Results: Second Time Step**

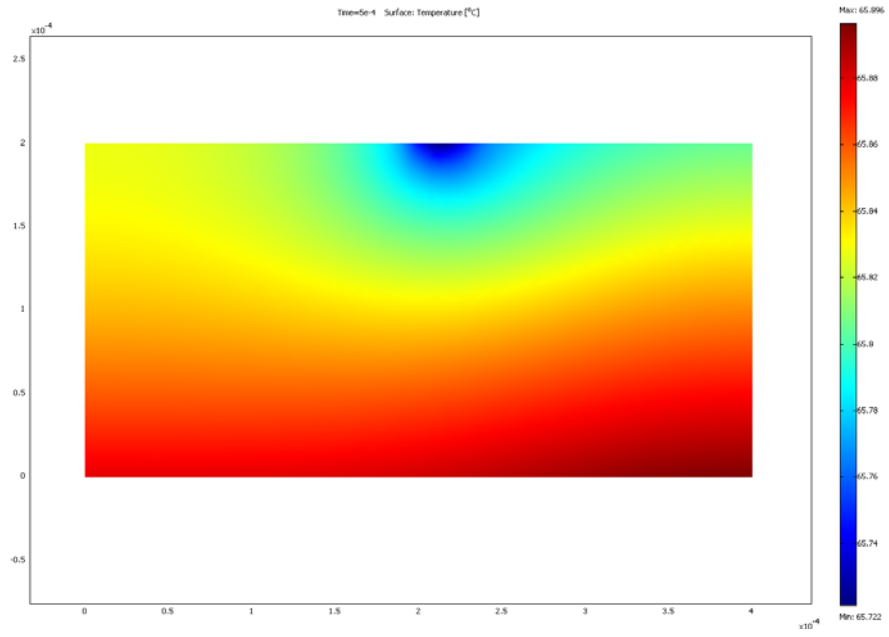**Figure 63: Sapphire Heater Simulation Results: Third Time Step**

Figure 64: Sapphire Heater Simulation Results: Fourth Time Step
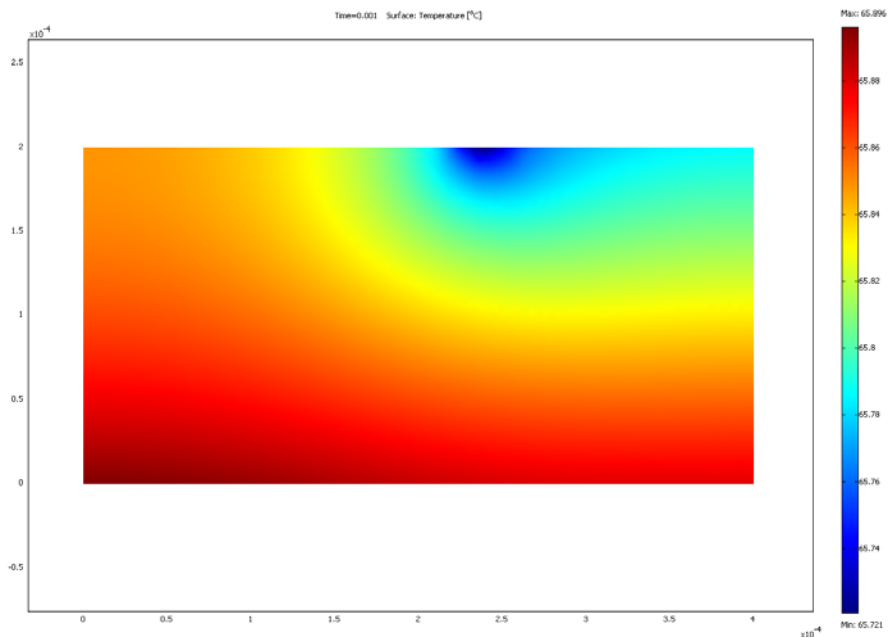

Figure 65: Sapphire Heater Simulation Results: Final Time Step

REFERENCES

[1] Carey, Van P., 1992, *Liquid-Vapor Phase-Change Phenomena*, Hemisphere Publishing Corporation, New York.

[2] Incropera, F. P., DeWitt, D. P., Bergman, T. L., and Lavine, A. S., 2007 *Fundamentals of Heat and Mass Transfer*, 6th edition, John Wiley & Sons, New Jersey.

[3] Rini, D., Chen, R.-H., and Chow, L.C., 2001, "Pool Boiling Characteristics Using FC-72," Experimental Heat Transfer, **14**(1), pp. 27-44.

[4] Moore, F. D. and Mesler, R. B., 1961, "The Measurement of Rapid Surface Temperature Fluctuations During Nucleate Boiling of Water," AIChE Journal, **7**(4), pp. 620-624.

[5] Rogers, T. F. and Mesler, R. B., 1964, "An Experimental Study of Surface Cooling by Bubbles During Nucleate Boiling of Water," AIChE Journal, **10**(5), pp. 656-660.

[6] Cooper, M.G. and Lloyd, A.J.P., 1969, "The Microlayer in Nucleate Pool Boiling," International Journal of Heat and Mass Transfer, **12**, pp. 895-913.

[7] Sako, M. and Kikuchi, Y., 1997, "Bubble Growth and Transient Heat Transfer at the Onset of Boiling," Heat Transfer-Japanese Research, **26**(7), pp. 484-492.

[8] Yaddanapudi, N. and Kim, J., 2001, "Single Bubble Heat Transfer in Saturated Pool Boiling of FC-72," Multiphase Science and Technology, **12**(3-4), pp. 47-63.

[9] Demiray, F. and Kim, J., 2004, "Microscale Heat Transfer Measurements During Pool Boiling of FC-72: Effect of Subcooling," International Journal of Heat and Mass Transfer, **47**, pp. 3257-3268.

[10] Myers, J. G., Yerramilli, V. K., Hussey, S. W., Yee, G. F., and Kim, J., 2005, "Time and Space Resolved Wall Temperature and Heat Flux Measurements During Nucleate Boiling With Constant Heat Flux Boundary Conditions," International Journal of Heat and Mass Transfer, **48**, pp. 2429-2442.

[11] Moghaddam, S. and Kiger, K. T., 2006, "Microscale Study of the Boiling Process in Low-Surface-Tension Fluids," Proceedings of ASME International Mechanical Engineering Congress and Exposition, Chicago, Illinois.

[12] Buchholz, M., Auracher H., Luttich, T., and Marquardt, W., 2006, "A Study of Local Heat Transfer Mechanisms Along the Entire Boiling Curve By Means of Microsensors," International Journal of Thermal Sciences, **45**, pp. 269-283.

[13] You, S. M., Hong, Y. S., Simon, T. W., and Bar-Cohen, A., 1995, "Effects of Dissolved Gas Content on Pool Boiling of a Highly Wetting Fluid," Journal of Heat Transfer, **117**, pp. 687-692.

[14] Zhang, X., Choi, H., Datta, A., and Li, X., 2006, "Design, Fabrication, and Characterization of Metal Embedded Thin Film Thermocouples with Various Film Thicknesses and Junction Sizes," Journal of Micromechanics and Microengineering, **16**, pp. 900-905.

[15] Tong, H. M., Arjavalingam, G., Haynes, R. D., Hyer, G. N., and Ritsko, J. J., 1987, "High-Temperature Thin-Film Pt-Ir Thermocouple with Fast Time Response," Review of Scientific Instruments, **58**(5), pp. 875-877.

[16] Guo, Z. and El-Genk, M.S., 1994, "Liquid Microlayer Evaporation During Nucleate Boiling on the Surface of a Flat Composite Wall," International Journal of Heat and Mass Transfer, **37**(11), pp. 1641-1655.

[17] Anderson, T.M. and Mudawar, I., 1989, "Microelectronic Cooling by Enhanced Pool Boiling of a Dielectric Fluorocarbon Liquid," Journal of Heat Transfer, **111**, pp. 752-759.

[18] Reed, S.J. and Mudawar, I., 1999, "Elimination of Boiling Incipience Temperature Drop in Highly Wetting Fluids Using Spherical Contact with a Flat Surface," International Journal of Heat and Mass Transfer, **42**, pp. 2439-2454.

[19] Marto, P.J. and Lepere, V.J., 1982, "Pool Boiling Heat Transfer From Enhanced Surfaces Due to Dielectric Fluids," Journal of Heat Transfer, **104**, pp. 292-299.

[20] Hsu, Y.Y., 1962, "On the Size Range of Active Nucleation Cavities on a Heating Surface," Journal of Heat Transfer, pp. 207-213.

[21] Park, K.-A. and Bergles, A.E., 1986, "Boiling Heat Transfer Characteristics of Simulated Microelectronic Chips with Detachable Heat Sinks," Proceedings of the Eighth International Heat Transfer Conference, San Francisco, California, pp. 2099-2104.